Master's Final Report

Master on Physics and Physical Technologies

&

Master on Renewable energy and advanced materials

SANS and μSR studies of magnetic textures in chiral magnets

Author

María Sánchez Echeverría

Director

Jesús Javier Campo Ruiz

Faculty of Sciences

2023

Contents

1 Introduction and goals **1**

2 Previous knowledge **3**
2.1 Magnetism in chiral solids 3
2.2 Previous experimental techniques 5
2.2.1 Vibrating Sample Magnetometer (VSM) 5
2.2.2 Neutron Scattering 6

3 Muon Spin Rotation (μSR) **10**
3.1 Setting and experiment 13

4 Simulation software development **15**
4.1 Experimental setting and MnSi nuclear structure 16
4.2 Magnetic model. 4 Helixes magnetic structure 17
4.3 Muon implantation site 18
4.4 Local field at muon's site 18
4.4.1 Demagnetisation Field. $\vec{B}_{dem}$ 19
4.4.2 Hyperfine Field. $\vec{B}_{RKKY}$ 19
4.4.3 Dipolar Field. $\vec{B}_{dip}$ 20
4.4.4 Lorentz Field. $\vec{B}_{Lor}$ 20
4.4.5 Total Field. $\vec{B}_{loc}$ 21
4.5 Larmor equation 22

5 First results and future work **23**

A Pyhton Code **26**

Chapter 1

Introduction and goals

Being able to master materials with specific attributes and implement them to our day a day life has improved many aspects of our society, from medicine to construction, energy or communications. Materials have been, and still are, the starting point for every major development in history. From the control of fire to the metal ages, the use of paper, magnets as orientation devices and, later on, the discovery of piezoelectric, radioactive or superconductor materials. Each of them has brought us one step closer to the silicon and plastic based era where we stand now, and this kind of breakthrough discoveries are what push progress forward.

Up until now, we have allowed ourselves to think in a very profit-focused way: cheaper products, faster to build, lighter, smarter... but now the table has turned. Now we are ankles deep into a global climate crisis, not to mention a shortage of many materials that are crucial to our way of life. Those parameters that defined the industrialization era are not longer valid and others like "environmentally and energetically friendly" or "renewable or recyclable" have to be promoted to the front line.

This search for materials that fit our new needs has stimulated the growth of materials science.

One of the many topics that are being explored is Magnonics. Thought to be an utter revolution in the technology and communication field, magnonics hopes to redefine the way we transmit, storage and process information. Currently, electronics and spintronics are mainly based on the movement of charges, which leads to an energy loss via the Joule effect. In magnonics, the coding of information would relay on the movement of magnetic moment structures, avoiding said energy loss. This promising field of study has skyrocketed the study of chiral magnets, proposed as the perfect support for this technology, boosting all kind of experiments that aim to characterize their structure and magnetic properties.

The M4 (Multi-functional Magnetic Molecular Materials) research group followed this line of investigation and published in 2017 a theoretical model ([1]) for cubic helimagnets that predicts the existence of a skyrmionic phase [2] at low temperatures, near the transition line of the material, called Phase A (there was an already known Phase A near the critic temperature of the material and low magnetic field $\vec{H}$) and a new and unknown magnetic phase, called Phase B, that doesn't fit any of the previous models (conical helicoid, simple ferromagnet or skyrmionic lattice). We can see a schematic phase map on Figure 1.1.

This new phases appear due to the instability of the stationary points of the energy functional, as explained on the mentioned article. After this publication, the M4 research group carried out a set of experiments characterizing two cubic crystals with very similar structures, a $MnSi$ and a $Fe_{1-x}Co_xSi$.

The macroscopic magnetic properties of the $Fe_{1-x}Co_xSi$ were obtained via VSM (Vibrating sample-magnetometer) from which a phase diagram was drawn, hinting at low temperatures

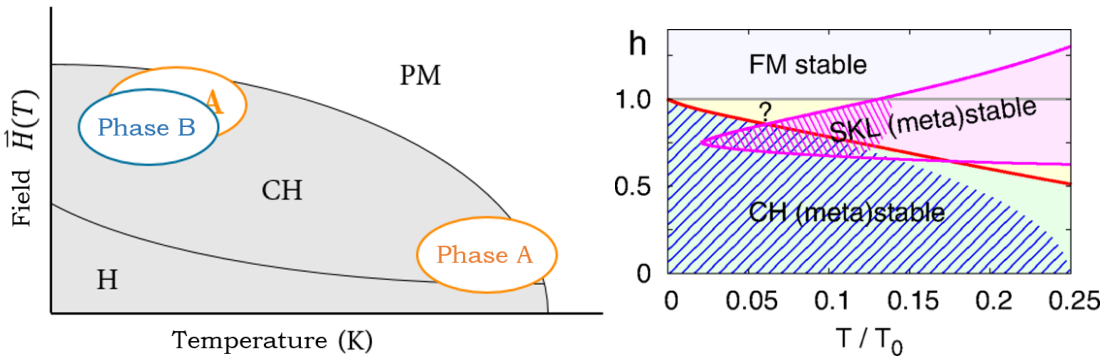

Figure 1.1: Phase diagram presented by Campo y Laliena [1]. Conical helicoid and skyrmionic lattice structures are valid for blue and pink striped areas respectively. Region (?) presents an unknown phase.

the existence of the new Phase B, but nothing leading to the new Phase A. SANS experiments were then performed in order to determine the nature of the proposed Phase B. The preliminary results of the SANS experiment were obtained on 2022 and, although the abnormalities that were observed through VSM at low temperature, no skyrmions nor new phase were found. This does not contradict the existence of a new magnetic phase, since it could be one that presents the same pattern as a conical helicoid when looked at using neutrons.

The study of MnSi followed the same approach. The VSM results showed that, for all three directions $< 100 >< 110 >$ and $< 111 >$ the typical A-Phase near T_c was observed, but only on the $\vec{H}|| < 111 >$ direction, a flat-valley-like anomaly appeared on the magnetization measurements at low temperatures, as stated in ([3]), the new B-Phase. No secondary A-Phase was seen at low temperatures near the transition.

This led the group to perform SANS experiments on the $< 111 >$ direction, specifically studying the region where the new B-Phase should materialize. No difference on the wave's vector modulus or direction was perceived, obtaining the imprint of the typical conical helicoid phase, however, changes on the expected decrease of the intensity of the peaks did appear. All this information suggests that the B-Phase is not a skyrmion lattice nor a normal conical helicoid.

Several models that fit these results had been theorised, but magnetometry and neutron scattering could not give any further information. At that point, complementary techniques were needed for the sake of sheding some light to the B-Phase puzzle.

During 2022 μSR (Muon spin rotation) experiments were carried out at TRIUMF's facilities in Canada. Since this technique requires the existence of a magnetic model to compare the results with, the main goal of this work will be to develop a simulation of the magnetic structure of the crystal around the muon's implantation site. Then, the parameters of the model will be changed in order to fit the data provided by the experiment. The model we will be simulating, as stated in [3], consists on the propagation of 4 helixes with one of them being out of phase by $2^{\text{º}}$.

The structure of this work is as follows: in Chapter 2 we will review general concepts of magnetism to then frame the models and structures we are interested in. We will then pay attention to some of the techniques used for the characterization of the samples, such as SQUID, VSM, SANS and, finally and more in depth, μSR. Once the theory is clear, we will present the sample used as well as the experimental set-up. The last chapter will cover the simulation code and some fitting results.

Chapter 2

Previous knowledge

2.1 Magnetism in chiral solids

The study of the magnetic properties of matter has interested human beings since ancient times; however, explaining the origin of such behaviors continues to be an active field for modern science.

The response of a material to an external magnetic field depends on whether or not it has an atomic magnetic moment. This moment has a nuclear component and an electronic component, which involves the electron's angular momentum $\vec{L}$ and its intrinsic spin $\vec{S}$. Depending on how the material responds to the application of the field, we can differentiate between several types of magnetism: diamagnetism, present in all solids and caused by an induced magnetic moment, and paramagnetism, caused by the existence of a magnetic moment originated by the angular momentum J of the unpaired electrons.

Let's assume an interatomic interaction that takes into account both the Coulomb electric interaction and the Pauli exclusion principle. This is the cause of other types of magnetism that could eventually produce magnetic Long Range order (LRO), shown in Figure 2.1. Depending on the position that implies the minimum energy between two magnetic moments of spin, we obtain different types of magnetic order: ferromagnetism, antiferromagnetism, ferrimagnetism, etc.

Thus, the interaction between two atoms mediated by the exchange coefficient J is defined as:

$$H = -\sum_{i,j} J_{ij} \vec{S}_i \vec{S}_j \tag{2.1}$$

Where $\vec{S}i, j$ are the moments of each atom and Jij is the value of J between the j and i atoms.

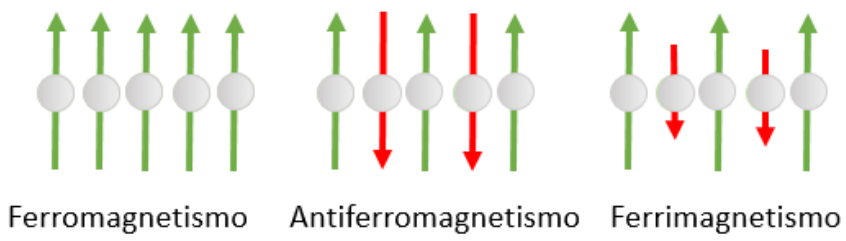

Figure 2.1: Representación esquemática de la orientación de espín en configuración ferro, antiferro y ferrimagnética

Materials with magnetic order are characterized by the existence of a critical temperature T_c, above which the material loses its long-range order. Additionally, below this critical temperature,

ordered magnetic domains may appear, separated by domain walls, so that although a well-defined magnetization appears within a domain, the material may not exhibit total spontaneous magnetization.

So far, we have considered that two spins can be parallel or antiparallel. This model has been useful for understanding electronic exchange. In addition to the exchange interaction, whose energy minimum is found with parallel or antiparallel ordering of the magnetic moments of spin, there are other interactions that will influence the final ordering of the system.

One of them is the Dzyaloshinskii-Moriya (DMI) interaction. This has its origin in the antisymmetric part of the spin-orbit coupling function, so it is zero in centrosymmetric crystals. The DMI is described by expression 2.2, in which the energy minimum corresponds to the positions of the spin magnetic moments perpendicular to each other. Typically, the intensity of the DMI, D, is weaker than the intensity of the exchange interaction J. The presence of both interactions gives rise to helical magnetic structures, whose rotation angle is proportional to the ratio of the intensities of the interactions D/J, or 'canted' structures, as shown in Figure 2.2.

$$H = \sum_{i,j} \vec{D}_{ij}(\vec{S}_i \times \vec{S}_j) \tag{2.2}$$

Another possible origin of a non-collinear magnetic structure arises from extending the exchange interaction beyond first neighbors. This gives rise to a phenomenon called frustration. In this situation, a magnetic moment is ordered so as to minimize the energy taking into account the exchange with nearby moments, not just its immediate neighbor. This results again in a helix, explaining why these structures can be observed in centrosymmetric crystals where DMI is not involved.

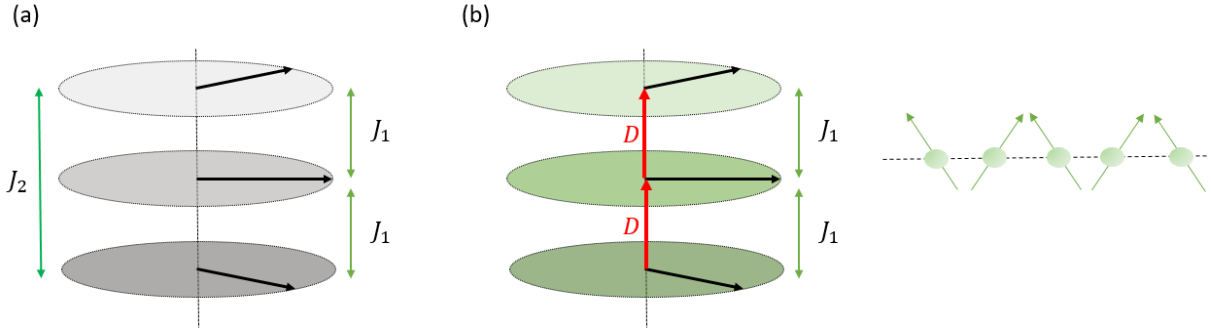

Figure 2.2: (a) Formación de una estructura helicoidal debida a la frustración y (b) Formación de una estructura helicoidal y canted debido a la presencia de DMI

The presence of an external magnetic field in a specific direction results in adding a Zeeman term to the Hamiltonian, leading to conical-helical structures if the field is parallel to the axial axis, or chiral soliton networks if the field is applied perpendicular to the helix axis. Justifying why these structures can also be observed in centrosymmetric crystals where DMI is not involved.

To mathematically describe these structures, a function is defined that assigns, for each atom dm and nuclear cell l in space, the magnetization $\vec{M}_{l,dm}$ at that point. This function can be expressed as a set of plane waves through Fourier coefficients defined as $\vec{S}_{\vec{K},dm}$ (equation 2.3). The vector of these plane waves is called the magnetic propagation vector $\vec{K} = (\alpha, \beta, \gamma)$ and reflects the relationship between magnetic moments located in different nuclear cells of the crystal, that is, it defines the relationship between the magnetic and nuclear cells. If α,β,$\gamma \in \mathbb{Q}$, the structure is called commensurate, otherwise it will be incommensurate.

$$\vec{M}_{l,dm} = \sum_{\vec{K}} \vec{S}_{\vec{K},dm} e^{-i2\pi\vec{K}\vec{R}_l} \tag{2.3}$$

The indices dm and l in equation 2.3 label the atom dm within the cell l. In Figure 2.3, the values of l= 1,2,3 can be seen, while since there is only one atom per cell, it is not necessary to indicate dm.

In Figure 2.3, the propagation vector $\vec{K}$, which as we have already explained, marks the relationship or change of equivalent magnetic moments in different cells, will take a value of $\vec{K} = (0, 0, \frac{1}{2})$ in the case of an antiferromagnetic ordering system since the magnetic moment repeats its ordering every 2 nuclear cells of the crystal (in the case of a single magnetic atom per nuclear unit cell). To describe a ferromagnetic system, $\vec{K} = (0, 0, 0)$ is used because the moment does not vary, that is, the magnetic cell coincides with the nuclear cell.

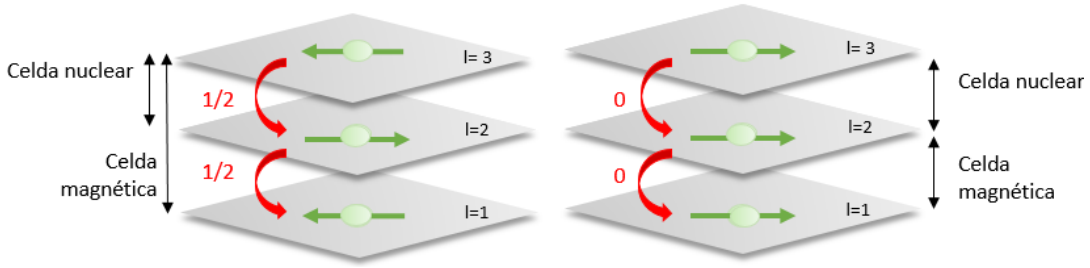

Figure 2.3: Celda magnética frente a celda nuclear en sistema antiferromagnético (izq) frente a ferromagnético (dcha)

The simplest Hamiltonian to describe a chiral magnetic system is shown in equation 2.4, where J, D, B, and S are parameters corresponding to the intensity of the exchange interaction, DMI, external field, and magnetic moment.

$$H = -\sum_{i,j} J_{ij}\vec{S}i\vec{S}j - \sum_{i,j} \vec{D}ij(\vec{S}_i \times \vec{S}j) - g\mu_B \sum_i \vec{S}_i\vec{B} \tag{2.4}$$

The solutions of the Hamiltonian like the above for cubic magnets include helical magnetic structures, conical helices, simple ferromagnetics, and skyrmionic lattices.

2.2 Previous experimental techniques

The same subject can be investigated in many different ways, each of them bringing to light different properties or aspects of a sample, so that as much information as possible is obtained. The complementary techniques employed over the course of this study are going to be briefly introduced in the following pages, that way, the reader can follow the same steps the group took and how each of them led to a new piece of information.

2.2.1 Vibrating Sample Magnetometer (VSM)

This instrument measures magnetic properties of a sample based on Faraday's law of induction. A magnetic sample is placed inside a constant magnetic field created with an electromagnet. The magnetic dipolar moment of the sample will try to align with the external field. The sample is then forced to vibrate, generally by a piezoelectric actuator, so that the magnetic field created by the sample's dipole moment changes with time when moved up and down.

This changing magnetic field induces a current in the so called pickup coils. These sensors are placed in a way on which the external magnetic field generated by the electromagnet is cancelled and only the one created by the sample is taken into account. The voltage induced in the pick-up coils is proportional to the sample's magnetic moment and does not depend on the strength of the applied magnetic field.

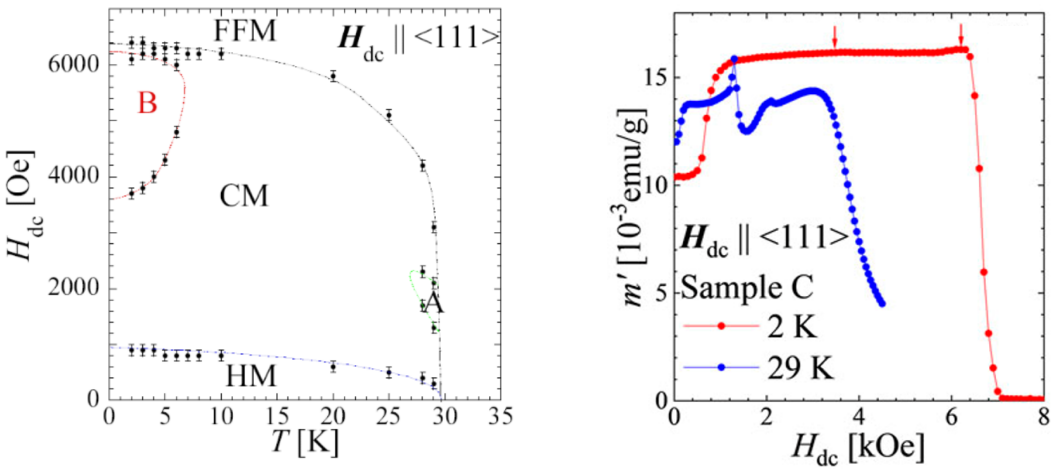

Figure 2.4: (left) Phase diagram of MnSi sample with $\vec{H}|| < 111 >$ from VSM measurements. (right) Magnetization versus field at 2K and 29K with $\vec{H}|| < 111 >$ from [3]

In Figure 2.4 we can see, at temperatures close to the material's $T_c = 30K$, an A-Phase region as expected. Besides that, at temperatures below 7 K and fields between $4000 - 6000Oe$, a possible B-Phase, hinted by a depression at the magnetization measurements.

2.2.2 Neutron Scattering

This technique allows the study of nuclear and magnetic structures ranging in size from sub-$\mathring{A}$ to micrometers (μm) and movements with energies ranging from neV to meV, which places us in the appropriate energy range for the study of magnetic structures and their dynamics. The neutron interacts with matter in two ways: through nuclear strong interaction with nuclei and through electromagnetic interaction with unpaired electrons and those nuclei that possess magnetic moment. The first interaction will be used to define the nuclear structure, while the second will provide information about the magnetism of the sample.

A neutron scattering experiment consists of irradiating the study system with a neutron beam and counting the number of neutrons scattered in a certain direction and energy. This information is given by the double cross-section:

$$\frac{d^2\sigma}{d\Omega_{\vec{k}f} dE_f} = \frac{k_f}{k_i}(\frac{2\pi m}{h})^2 | < \vec{k}_f \sigma_f; \psi_f | H_{int} | \vec{k}_i \sigma_i; \psi_i > |^2 \delta(E\psi_i - E\psi_f + h\nu) \quad (2.5)$$

The neutron-matter interaction is described by the interaction Hamiltonian, denoted by H_{int}. The states before and after the interaction are distinguished by the indices i and f, respectively. The variable $\vec{k}$ defines the wave vector of the beam. The incident wave is a plane wave. The wave that describes the scattered beam is spherical; however, due to the large distance between the sample and the detector, we can approximate it to a plane wave. From both wave vectors, we can define the scattering vector $\vec{q} = \vec{k}_f - \vec{k}_i$, which is related to the transfer of momentum between neutron and sample, and the spin state of the beam is fixed by σ. The last term $h\nu$ can be defined in terms of the neutron energies as $h\nu = E_i - E_f$. On the other hand, the state of the sample is described by ψ, and $E\psi$ is its energy.

The strong interaction is intense and of very short range, only effective when the neutron is close to the atomic nucleus. The potential employed to reproduce these conditions is the Fermi pseudo-potential (expression 2.6), where $\vec{r_d}$ is the distance between the neutron and the nucleus d.

$$V_d(\vec{r}_d) = \frac{2\pi\hbar^2}{m} b_d \delta(\vec{r}_d) \tag{2.6}$$

The pseudo-potential depends on the parameter b_d, called the scattering length. The scattering length is a constant independent of the directions of the beam. It is different for each nucleus and provides information about how the interaction is. It is a complex number whose real part is the scattering amplitude. This is the reason why neutron scattering is effective in distinguishing isotopes of the same element.

To mathematically describe the sample structure, we introduce the pair correlation function (equation 2.7). This function indicates the probability of finding two atoms at a distance r at a given time.

$$G(\vec{r}, t) = -\frac{1}{N} \sum_{i,j} < \delta(\vec{r} - [\vec{r}_i(0) - \vec{r}_j(t)] > \tag{2.7}$$

The Fourier transform in time and space of the pair correlation function is the dynamic structure factor $S(\vec{q}, \nu)$, which provides information about the position of the atoms and is related to the coherent part of the scattering function $I_n^{coh}(\vec{q}, \nu)$. When it is integrated over all energies, we end up with the elastic part of the scattering.

$$I_n^{coh}(\vec{q}, \nu) = \frac{d^2\sigma}{d\Omega dE_f} = \frac{\sigma^{coh}}{4\pi} \frac{k_f}{k_i} N_n \vec{S}(\vec{q}, \nu) \tag{2.8}$$

$$I_n^{coh}(\vec{q}) = \frac{(2\pi)^2}{V_0} \sum_{\vec{G}} \delta(\vec{G} - \vec{q}) |N_q|^2 \tag{2.9}$$

This way, we can express the number of scattered neutrons in a direction, collected in equation 2.9 and known as the coherent scattering law, where $|N_q|$ is the nuclear structure factor, and $\vec{G}$ labels the nodes of the reciprocal lattice. This indicates that we will have scattering points when the scattering vector coincides with a node of the reciprocal lattice, i.e., $\vec{G} = \vec{q}$. The intensity of these peaks is controlled by the nuclear structure factor, defined as:

$$N_{\vec{q}} = \sum_m b_m e^{i2\pi\vec{q}\vec{r}_m} e^{-W_m(\vec{q})} \tag{2.10}$$

The label m corresponds to an atom of the lattice, so the structure factor depends on the scattering length corresponding to that atom, a phase related to the position of the atom, and a Debye-Waller factor, which reproduces the small displacements of the atom m with respect to its equilibrium position in the lattice.

So far we have considered the sample's structure but we have yet to consider the magnetic part. The law of magnetic scattering can be written as shown in equation 2.11. This expression has been simplified by defining the magnetic structure factor $\vec{M}_{\vec{q}\vec{K}}$ (equation 2.12). The component perpendicular to the scattering vector $\vec{q}$ is called the magnetic interaction vector, and the square of its modulus gives the intensity of the diffraction peaks.

$$I_m^{coh}(\vec{q}) = \frac{(2\pi)^2}{V_0} \sum_{\vec{G},\vec{K}} \delta(\vec{G} - \vec{q} - \vec{K}) |\vec{M}\perp \vec{q}|^2 \quad \text{where} \quad |\vec{M}\perp \vec{q}| = |\hat{q} \times (\vec{M}_{\vec{q}\vec{K}} \times \hat{q})| \tag{2.11}$$

$$\vec{M}_{\vec{q}\vec{K}} = \sum_{dm,\vec{K}} F_{dm}(\vec{q}) T_{dm}(\vec{q}) e^{i2\pi\vec{q}\vec{r}_{dm}} \vec{S}\vec{K} dm \tag{2.12}$$

where $\vec{S}_{\vec{K}dm}$ denotes the Fourier coefficients. The diffraction peaks will no longer occur at points where $\vec{q} = \vec{G}$, but satellites will appear at distances $\vec{K}$ from the nuclear scattering peaks.

The total intensity for unpolarized scattered neutron beams, taking into account both the nuclear and magnetic parts, is given by:

$$I(\vec{q}) = |\vec{M}\perp \vec{q}|^2 + |N\vec{q}|^2 \quad \text{for} \quad \vec{q} = \vec{G} \pm \vec{K} \tag{2.13}$$

Small angle neutron scattering

Any magnetic structure can be described according to the propagation vector $\vec{K}$ formalism explained in the previous section. A smaller value of this vector corresponds to a larger number of nuclear cells contained in each magnetic cell. In other words, the magnitude of the $\vec{K}$ vector is related to the spatial period of the structure.

Magnetic diffraction maximums are fixed at points that satisfy $\vec{q} = \vec{G} \pm \vec{K}$. For this reason, if the structure being studied has a very small propagation vector $\vec{K}$, we will find the diffraction peaks of the satellites at very small values of the scattering vector, having to resort to low-angle or SANS (small angle neutron scattering) techniques that specialize in neutron scattering at small values of $\vec{q}$. This technique is explained at depth in [4].

The structures that we wanted to observe are magnetic helices formed by DMI so that the rotation angle at each loop of the helix is given by the ratio D/J which is very small, so a single period of the helix will occupy many nuclear cells.

There are two basic settings depending on the relative direction between the incident beam $\vec{k}_i$ and the applied field $\vec{H}$. As we have discussed in the previous section, the scattering vector $\vec{q}$ is defined as $\vec{q} = \vec{k}_f - \vec{k}_i$, confined to the detector plane. The intensity of the diffraction peaks is proportional to the square modulus of the magnetic interaction vector $\vec{M}_{\perp\vec{q}}$. Thus, the appearance or not of diffraction peaks will depend on two factors: that the value of $|\vec{M}\perp \vec{q}|$ is not zero and that the scattering vector $\vec{q}$ can satisfy the Dirac delta of equation 2.11 $\delta(\vec{G} - \vec{q} - \vec{K})$.

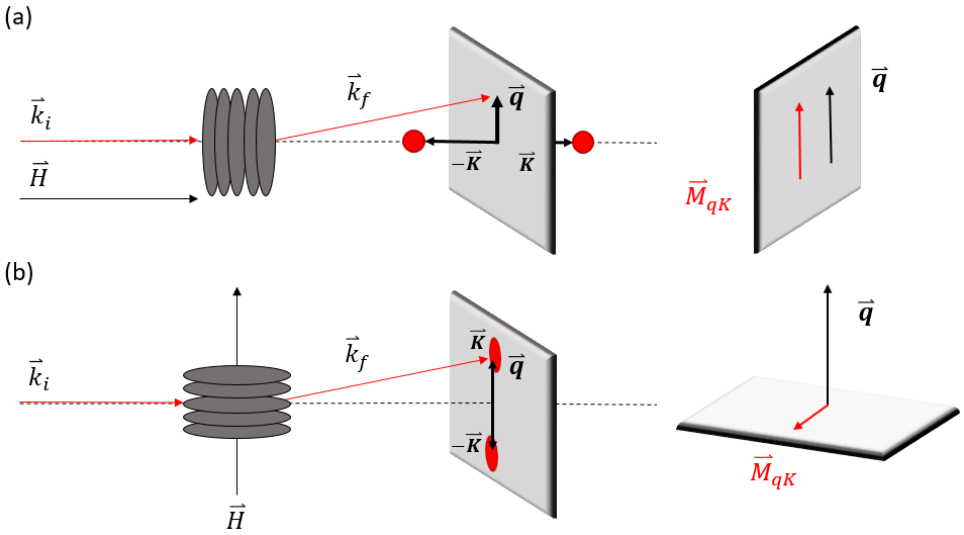

Figure 2.5: Possible settings of magnetic SANS experiment

Let us suppose a magnetic helical structure whose axis is parallel or perpendicular to the incoming neutron beam $\vec{K}_i$. The beam is fixed so that the point $\vec{G} = (0, 0, 0)$ is at the center of the detector, so that the diffraction maxima due to magnetic scattering or satellites appear at $\vec{q} = \pm\vec{K}$. Depending on the relative position between the incident beam and the applied field, we will have two possible results, illustrated in Figure 2.5:

a. Helical axis$||\vec{k_i}$: Since the $\vec{q}$ vector is contained in the detector plane, the point $(\vec{q} \pm \vec{K})$ is not accessible in this configuration, so no intensity peaks will be observed. In short, by irradiating with the beam parallel to the field, we cannot observe a helical structure whose axis is also parallel to the field.

b. Helical axis$\perp \vec{k_i}$: In this case, the vector $\vec{K}$ lies in the plane and is accessible to $\vec{q}$, which results in peaks of intensity in the detector. When the incident beam is perpendicular to the helical axis, we observe two diffraction peaks or satellites corresponding to $\vec{q} = \pm\vec{K}$, since, as seen in the figure, this configuration causes $\vec{K}$ to lie in the same plane as $\vec{q}$.

   If we put a field parallel to the helical axis and increase the magnetic field $\vec{H}$, the magnetic moments that form the helix will tilt, forming a conical helix. The component $\vec{M}_{\perp\vec{q}}$ decreases at the expense of the component parallel to the field, resulting in lower intensity.

The same can be used in order to observe other magnetic structures, resulting in different patterns. Both of the regions of interest (new A-Phase and unknown B-Phase) were explored in the MnSi sample using the time-of-flight type small and wide angle neutron scattering instrument TAIKAN [5] in the materials and life science facility (MLF) in J-PARC. The measurements were performed in thermal equilibrium condition at temperatures between 2 K and 35 K, and with applied magnetic fields below 0.8 T. The results did not show the new A-Phase, characterized by the 6 points pattern of the triangular skyrmionic magnetic phase. According to the magnetometry results, the new unknown phase appears below 7K and above 0.35T ([6]), where a conical helix pattern (Figura 2.6) was observed. The intensity of this pattern was lower than a classic conical helix magnetic structure, so that the existence of a new, non skyrmionic phase, is supported.

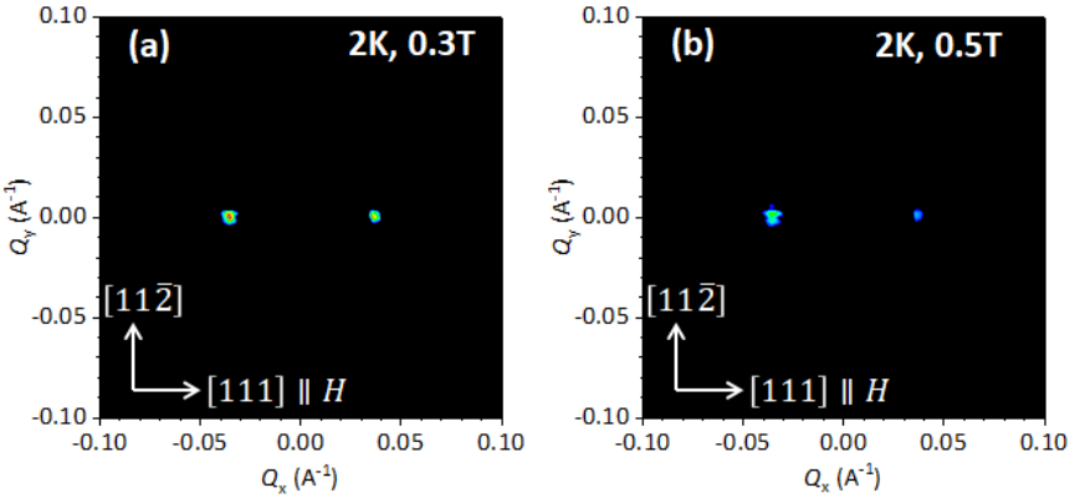

Figure 2.6: SANS pattern in the $\vec{H}||[111] \perp \vec{k_i}$ configuration (a) at 2 K, 0.3T and (b)2 K, 0.5T.

The distance from the center at which the satellites appear corresponds to the module of the propagation vector of the helical magnetic structure of MnSi:

$$|\vec{K}| = 0.035\mathring{A}^{-1} \tag{2.14}$$

Chapter 3

Muon Spin Rotation (μSR)

Every experimental technique that uses particles as a probe to study matter depends on that particle's properties and on the interactions of that particle with its surroundings (other particles, nuclei, electrons, atoms, molecules...). We have used neutrons because of their magnetic and strong force interactions with matter, now we are going to use another basic particle, the muon.

The muon is a fermion ($S = \frac{1}{2}$), negatively or positively charged, with a mass of 0.106 GeV (207 times heavier than that of the electron) which gives it an enormous penetration power. They can only be naturally found on Earth as a result of particles in the Earth's atmosphere colliding with cosmic rays high energy protons. They have a short lifetime of $2,2\mu s$ but, because they move close to the speed of light, they travel long distances before decaying. They decay via the weak interaction producing an electron, a neutrino and an anti-neutrino.

$$\mu^+ \longrightarrow e^+ + \nu_e + \bar{\nu}_\mu \tag{3.1}$$

$$\mu^- \longrightarrow e^- + \nu_\mu + \bar{\nu}_e \tag{3.2}$$

A very advantageous property of this decay is that, although neutrinos do not interact with matter, making it difficult to detect them, electrons or positrons are easier to see, and they are emitted following an angular distribution given in 3.3, characterised by an asymmetry that benefits the direction on which the magnetic intrinsic moment of the muon is pointing. The asymmetry parameter $a_{as}(\epsilon)$ varies with the positron kinetic energy ϵ as $\frac{2\epsilon-1}{3-2\epsilon}$.

$$W(\theta) = [1 + a_{as}(\epsilon)\cos(\theta)] \tag{3.3}$$

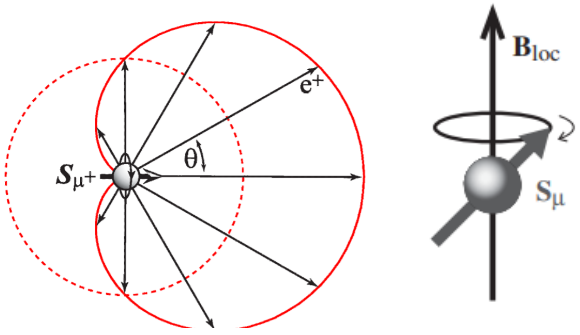

Figure 3.1: (Left) Polar diagram of the angular distribution $W(\theta)$ of positrons from muon decay. (Right) Schematic view of the Larmor precession of spin S_μ around B_{loc}.

The magnetic intrinsic moment is, like the mass or the charge, an intrinsic property of a particle and accounts for how it interacts with a magnetic field. It is a consequence of the existing spin momentum of a charged particle, which creates a small circuit of moving charges.

This settles the base for a μSR experiment. The main goal of the experiment is to follow the muon's spin polarization as it penetrates the sample and interacts with its magnetic local field B_{loc}. This is achieved by implanting polarized muons to the target and studying the direction on which the positron or electron is emitted, which gives us the polarization of the muon when it disintegrates. The final polarization, along with other variables previously obtained such as the muon's implantation sites inside the sample, the nuclear structure and magnetic model of the sample with a given propagation vector $\vec{K}$, gives us further information on how the magnetism inside our sample behaves and can help us refine or discard the model proposed.

The evolution of the polarization of the muon's spin inside the sample, from the initial polarized beam to the direction on which positrons are emitted is linked to B_{loc} through the Larmor equation (3.4). If the muon's spin S_μ precesses the local field B_{loc} (Figure 3.1) oriented at an angle θ from S_μ, the solution for the Larmor equation yields:

$$S_\mu(t) = S_\mu^{||}(0)\mathbf{u} + S_\mu^{\perp}(0)[\cos(\omega_\mu t)\mathbf{v} - \sin(\omega_\mu t)\mathbf{w}] \tag{3.4}$$

where the angular frequency is $\omega_\mu = \gamma_\mu B_{loc} = 2\pi\nu_\mu B_{loc}$. We have used a system with three orthogonal unit vectors **u, v, w** so that $\mathbf{u}||B_{loc}$ and $\mathbf{v}||S_\mu(0)$. This solution shows that the $S_\mu^{||}(0)$ component of S_μ, parallel to B_{loc} remains constant, while the perpendicular one rotates around B_{loc} with Larmor's angular frequency ω_μ. We define γ_μ as the gyromagnetic ratio and it is related to the muon's magnetic moment m_μ as:

$$m_\mu = \gamma_\mu \hbar S_\mu = \frac{\hbar}{2}\gamma_\mu \tag{3.5}$$

While the vector formalism we just presented is easier for understanding the concept, we will use the tensor formalism [7]. For this we are going to use a longitudinal operator $\mathbf{P}_L$ and two transverse ones $\mathbf{P}_{T1}$ and $\mathbf{P}_{T2}$ with which we can build a tensor $\mathbf{M}$(t) in order to express:

$$S_\mu(t) = \mathbf{M}(t)S_\mu(0) \tag{3.6}$$

$$\mathbf{M}(t) = \mathbf{P}_L(u) + \mathbf{P}_{T1}(u)\cos(\omega_\mu t) - \mathbf{P}_{T2}(u)\sin(\omega_\mu t) \tag{3.7}$$

$\mathbf{M}$(t) can be written through its Cartesian components, $M^{\alpha\beta}(t)$. Defining d_p as the direction of positron moment and i_μ as the direction of $S_\mu(0)$, we define polarisation as:

$$P_{i_\mu,d_p}(t) = \frac{\langle \mathbf{S}_\mu(t)\rangle}{S_\mu(0)} d_p \tag{3.8}$$

From where we can derive the final polarisation equation:

$$P_{i_\mu,d_p}(t) = \sum_{\alpha,\beta} \langle M^{\alpha\beta}(t)\rangle i_\mu^\beta d_p^\alpha \tag{3.9}$$

Once we know how the polarization of the muon behaves when affected by a local magnetic field $\vec{B}_{loc}$, we need to be able to relate that to the measurements taken by the detectors.

Let's consider the transverse-field geometry of a μSR experiment, since it is the one we will simulate in the next chapter. This setting is characterized by an external magnetic field applied perpendicular to the initial muon beam. Following Figure 3.2, when a muon crosses the "muon time 0 detector" at t_0, an electronic clock starts counting and stops when the positron reaches the "positron detector" at time t_n. We define $t_n = n\Delta t + t_0$, where "n" accounts for the number of digitization channels and Δt for the time resolution. An histogram representing the number of positrons detected against the time they have spent inside the sample can be built from this.

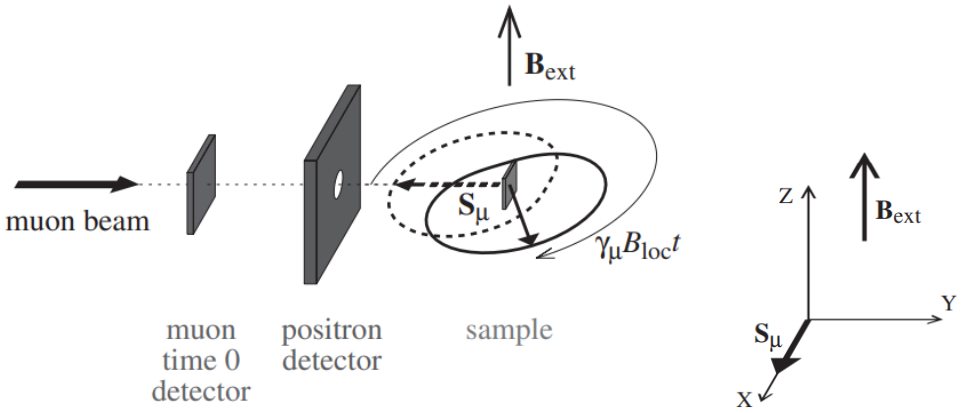

Figure 3.2: Transverse-field geometry of a μSR setting.

The positron count $N(t_n)$ can be expressed as equation 3.10 where the $\pm$ sign stands for the position of the detector (either in the "forward" direction, same direction as S_μ as represented in Figure 3.2, or in the "backward" direction, opposite to S_μ).

$$N_\pm(t_n) = N_0 exp(-t_n/\tau_\mu)[1 \pm a_0 P^{exp}(t_n)] \tag{3.10}$$

N_0 sets the scale of counts, τ_μ is the muon's lifetime, $P^{exp}(t_n)$ is the normalised polarisation function and a_0 is an experimental parameter that stands for the initial asymmetry, dependent of experimental conditions. We can distinguish two parts involved in the number of positrons detected. The exponential deals with the muon's natural decay over time while the second one concerns the polarization change. The previous equation can be manipulated into equation 3.11.

$$a_0 \eta_\mu P^{exp}(t_n) = \frac{N_+(t_n) - N_-(t_n)}{N_+(t_n) + N_-(t_n)}, \tag{3.11}$$

where the coefficient η_μ has been added for taking into account $P^{exp}(t < t_0)$. This way we experimentally obtain the polarisation function and relate it to the local magnetic field, as stated in equation 3.9

Now that we understand both how the emperimental setting attains the experimental polarization through time 3.11 and its relation with the precession of the muon spin around the local magnetic field 3.9 we can better comprehend the typical spectre of a μSR experiment, seen in Figure 3.3.

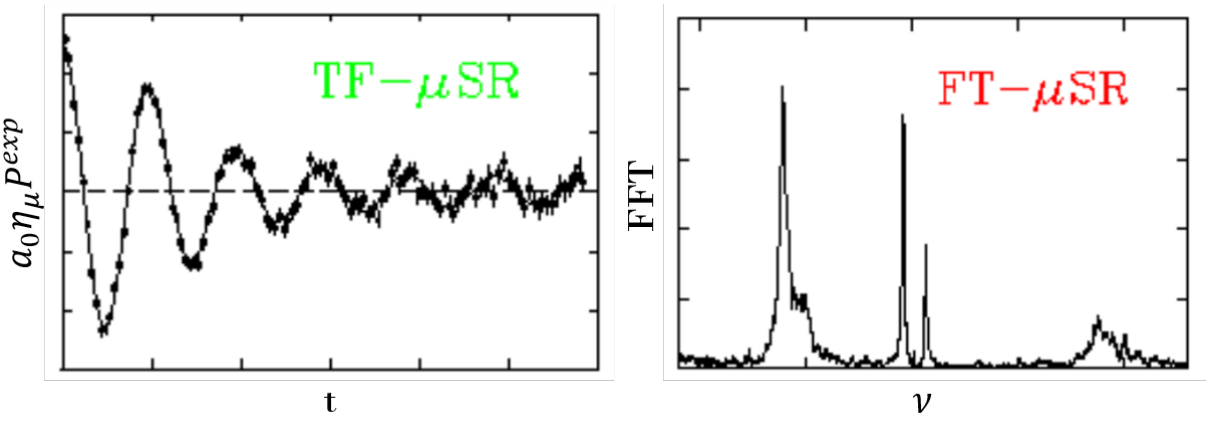

Figure 3.3: Typical spectre of a transverse field geometry μSR experiment

On the left, muon spin polarization is plotted against time and, following Larmor's equation 3.4, the spectre presents oscillations that are damped over time. The origin of the damping phenomena will be further explained on Chapter 4, Section 4.5, fully dedicated to Larmor's equation. Applying the Fourier Fast Transformation (FFT) to the Polarization-time data, we can plot the FFT intensity over frequency (right side of Figure 3.3). The frequency can be directly linked to the $\vec{B_{loc}}$ at the muon implantation site when it dies, so by looking at the position of the peaks in the $FT - \mu SR$ Figure, we obtain the module of the existing local field.

This technique has an extremely high sensitivity to internal magnetic fields, such as those with nuclear or electronic origin. It can also measure field fluctuations from $10^4 - 10^{12} Hz$ complementing Nuclear Magnetic Resonance (NMR). It has close to no limitations regarding sample sizing and works under a great variety of scenarios (temperature, magnetic fields up to 8T, electric fields, high pressure, irradiated with light...)

3.1 Setting and experiment

Transverse-field (TF) μSR experiments were carried out on the NuTime spectrometer installed on the M15 beamline of the centre for molecular and materials science (CMMS) facility at TRIUMF, Canada. M15 is equipped with dual spin-rotators, which serve both to separate positrons from the beam and to rotate the muon spin perpendicular to the beam direction.

We can take the sketch of the transverse geometry experiment (Figure 3.2) one step further, getting a closer look at how TRIUMF's real setting was designed (Fig 3.4). The muon's initial polarisation i_μ is contained in the x-axis and the field applied paralel to the z-axis. There are two sets of detectors, one in the y-axis, as shown in the figure, and another one along the x-axis.

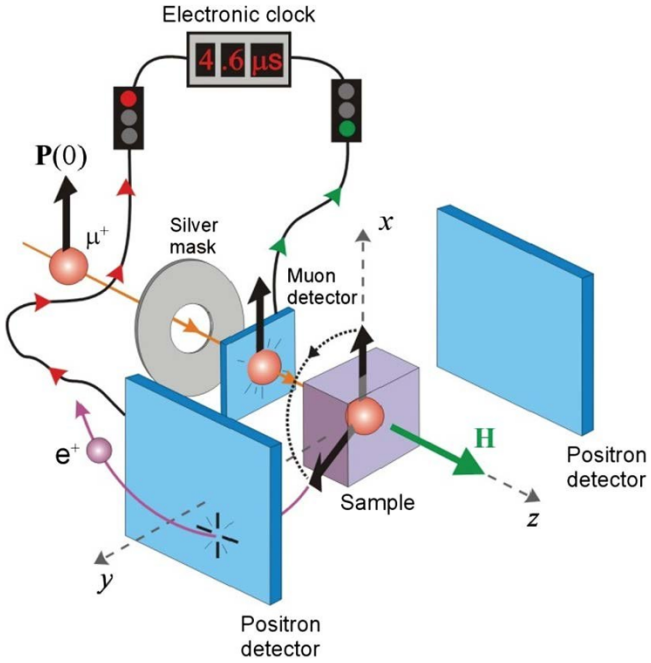

Figure 3.4: TRIUMF's μSR transverse geometry setting diagram

This means that we can measure the polarization change on the y-axis or x-axis, so that taking the x-axis as an example, our results would follow the expression below:

$$P_{X,X}(t) = \sum_{\alpha,\beta} \langle M^{\alpha\beta}(t) \rangle i_\mu^\beta d_p^\alpha = \langle M^{XX}(t) \rangle \tag{3.12}$$

Two crystals with the same size: $4.86 \times 3.65 \times 1.65\ mm^3$ were placed on top of a "muon-veto" scintillator. The crystals were then covered with a Ag foil (Figure 3.6. The muon veto together with the four positron counters form a cryostat insert and sample holder. TF μSR spectra with approximately $3{\cdot}10^7$ muon decay events were taken under conditions of zero field cooled ZFC, where the external magnetic field was applied by a 7 T superconducting magnet in the configuration: $\vec{B}||\langle 111\rangle \perp \vec{S}_\mu(0)$. The measurements were done in the temperature range 2 K to 50 K and field range 0 T to 0.75 T.

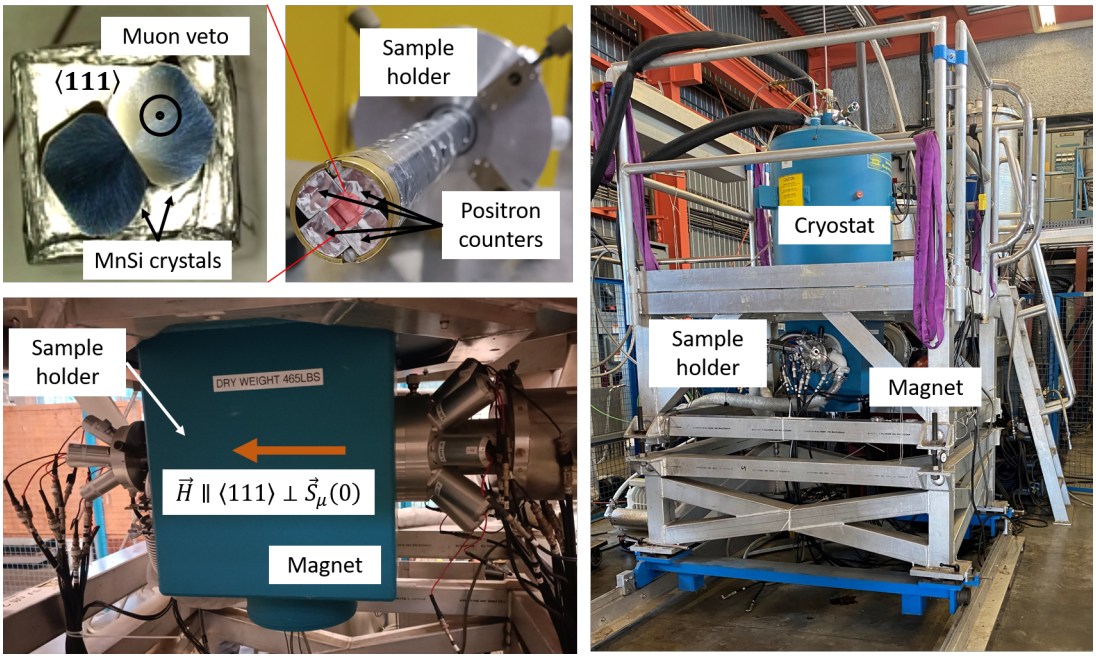

Figure 3.5: Sample covered in Ag foil and 4 positron counters

Figure 3.6: NuTime spectometer at M15 beamline, TRIUMF facility.

Chapter 4

Simulation software development

Once the experimental polarization has been measured, the results are to be compared to those of the simulation. This simulation has been designed to reproduce the sample's nuclear and magnetic structure based on previous experiments (VSM, SANS...). Once the sample's known parameters are fixed, we simulate a magnetic model and proceed to calculate the internal magnetic fields and their interaction with the simulated muons. By contrasting the outcome with the experimental results, we can perceive to which extent the proposed magnetic model reproduces what can be observed experimentally.

The code is written in Python and follows the diagram shown in Figure 4.1. A text file containing the value of every known variable allows the simulation of an experimental setup, a nuclear struscture, a magnetic structure and the muon implantation sites. Up to here,based on previous experimental results. The next step is to simulate the magnetic model we want to test, in our case, the 4 helix magnetic structure. The combination of the resulting magnetic structure and the muon's implantation sites will allow us to simulate the local magnetic field each muon senses before decaying. The last block uses the simulated $\vec{B}_{loc}$ and applies the larmor equation to the muon's spin, simulating their final polarization, $\vec{S}_{\mu f}^{Sim}$. This is then compared to the experimental final polarizations $\vec{S}_{\mu f}^{Exp}$ measured on the NuTime spectrometer.

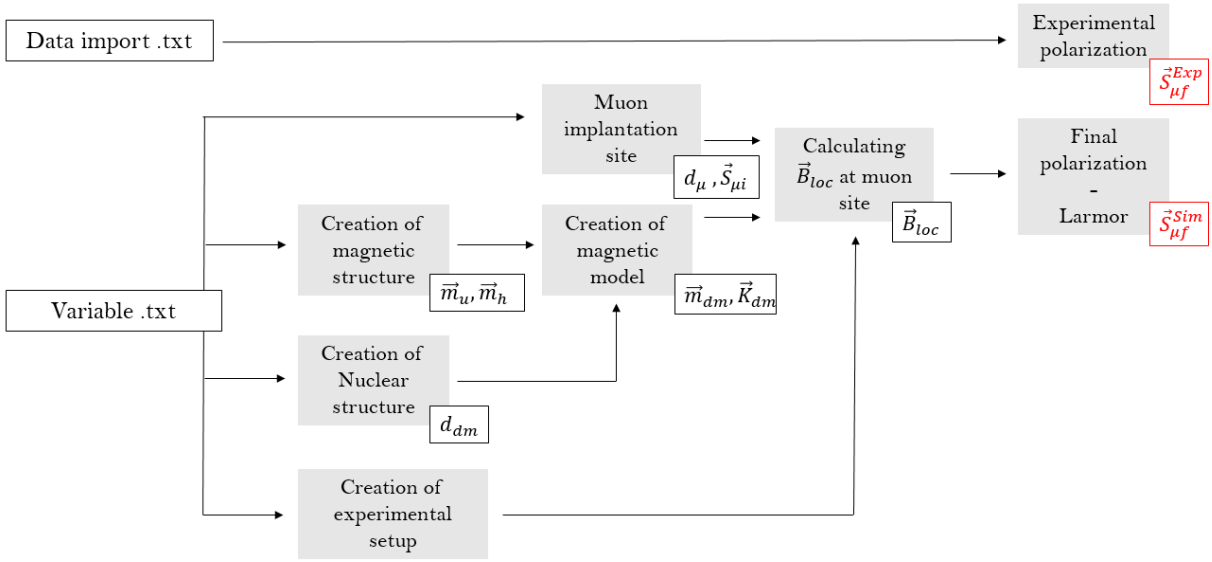

Figure 4.1: Simulation working diagram. "Variable.txt" provides the values needed for the simulation. "Data Import.txt" provides experimental results. d_{dm} is the position of the nuclear structure atoms, d_μ position of the muon, $\vec{m}_u$,$\vec{m}_h$ magnetic moments parallel and perpendicular to the propagation vector $\vec{K}$ and $\vec{S}_\mu$ is the polarization of the muon.

4.1 Experimental setting and MnSi nuclear structure

The first part of the simulation involves the axis and constant parameters throughout the experiment. The setting reproduces a transverse field geometry μSR experiment. The external field B_{ext} will be applied parallel to the sample's [111] direction, aligned with the z axis. The muon beam will follow the [$\bar{1}$10] direction, defining the x axis. The temperature and module of B_{ext} will be fixed at this stage of the simulation, covering ranges from 2-40K and 0-0,75T respectively.

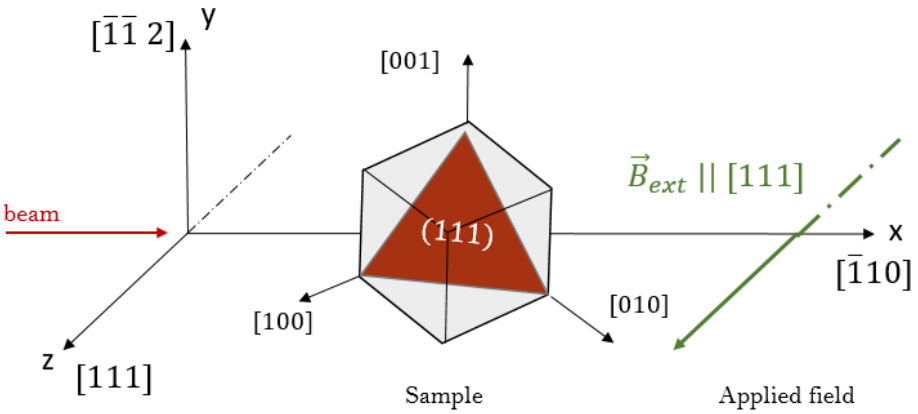

Figure 4.2: Transverse-field geometry setting with sample positioning.

The sample is a MnSi compound, a cubic crystal lattice with no inversion. The compound behaves as a paramagnet over 29K, while below this temperature spins create helical, conical, skyrmionic or simple ferromagnetic structures. Its unit cell is formed by 4 manganese atoms and 4 silicon ones, cristallizing in a $P2_13$ spatial group (No. 198) with a lattice parameter $a_0 = 4,558\mathring{A}$.

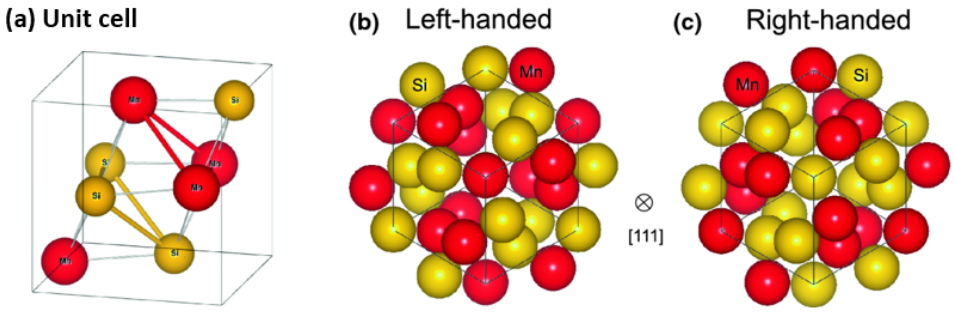

Figure 4.3: MnSi crystal structure.

Our attention is going to be focused on the manganese ions, occupying the 4a Wyckoff positions (x, x, x) with $x_{Mn} = 0,138$. Each position will be labeled as $\gamma = 1, 2, 3, 4$.

$$\vec{d}_{Mn}(\gamma = 1) \Longrightarrow (x_{Mn}, x_{Mn}, x_{Mn})$$
$$\vec{d}_{Mn}(\gamma = 2) \Longrightarrow (\tfrac{1}{2} - x_{Mn}, 1 - x_{Mn}, \tfrac{1}{2} + x_{Mn})$$
$$\vec{d}_{Mn}(\gamma = 3) \Longrightarrow (1 - x_{Mn}, \tfrac{1}{2} + x_{Mn}, \tfrac{1}{2} - x_{Mn})$$
$$\vec{d}_{Mn}(\gamma = 4) \Longrightarrow (\tfrac{1}{2} + x_{Mn}, \tfrac{1}{2} - x_{Mn}, 1 - x_{Mn})$$

4.2 Magnetic model. 4 Helixes magnetic structure

The magnetic model is key in this experiment. From the known conical helical magnetic structure that forms in the ordered phase of the crystal, we are going to simulate the de-phasing of the helices to then compare it to the experimental results. This magnetic model will define the magnetic fields the muon perceives when implanted and, therefore, the polarisation it acquires before decaying.

As explained in the first chapter, every magnetic structure can be defined through the magnetic propagation vector $\vec{K}$ formalism (Equation 2.3). In this formalism we define $\vec{S}_{\vec{k},d_m}$ as the Fourier coefficients. On our setting, the real part of $\vec{S}_{\vec{k},d_m}$ will be defined in the x-axis and the imaginary part in the y-axis, while $\vec{K}$ follows the z-axis. The value of its module is known thanks to previous SANS measurements (2.14)

$$K = |\vec{K}| = 0,035\mathring{A}^{-1}, \tag{4.1}$$

setting a wavelength $\lambda = \frac{2\pi}{K} = 180\mathring{A}$. We then define an helix originated in every manganese atom labeled "dm" inside a given unit cell labeled "d", by calculating the propagation vector $K_{d,d_m} = \vec{K}\vec{R}_{d,d_m}$, where $\vec{R}_{d,d_m}$ is the "d" atom, "dm" manganese position. For this, the software creates a loop that goes through the 4 manganese positions of a unit cell. For the manganese holding the γ Wyckoff position, we make a loop through every cell, defined by (a_i, b_i, c_i) with $a_i, b_i, c_i = 0, ..., N$, where N is the number of cells in one direction of the sample. Our sample has $N = 80$ cells in each direction. We start by fixing the a_i index, on the yz-plane, and define a sphere to limit the other b_i, c_i indexes as sketched in Figure 4.4. We are only calculating magnetic moments of manganese atoms close to the [111] direction.

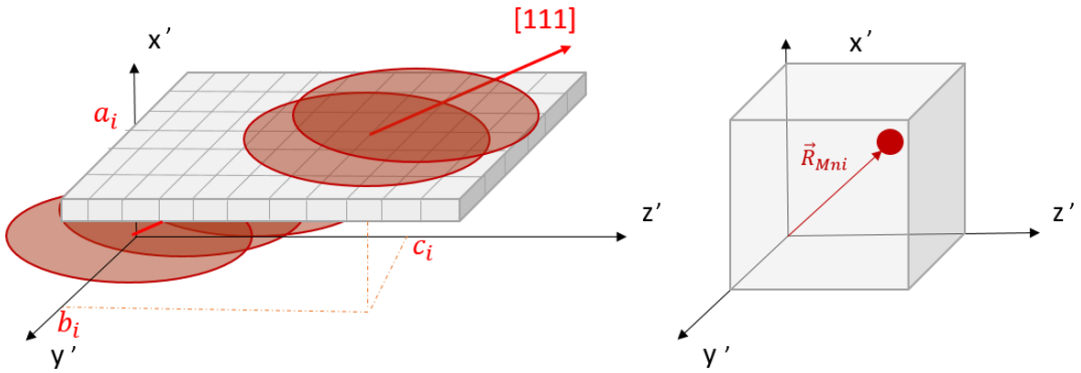

Loops for Mn "i" inside sample Mn "i" inside unit cell

Figure 4.4: Transverse-field geometry setting with sample positioning.

Once we calculate the exact position of the d_m manganese atom inside the $d = (a_i, b_i, c_i)$ cell, we obtain K_{d,d_m} propagation vector and, therefore, its magnetic moment $\vec{m}_{dm}$. It will have one component parallel to the z-axis (the direction of the propagation of the helix) named $\vec{m}_u$ and another one in the x-y plane, $\vec{m}_h$, defined as:

$$\vec{m}_{dm} = m_h\{\vec{S}^{Real}_{\vec{k},d_m}\cos(K_{d,d_m} + \phi_\gamma)\hat{x} \pm \vec{S}^{Imag}_{\vec{k},d_m}\sin(K_{d,d_m} + \phi_\gamma)\hat{y}\} + m_u\vec{B_{ext}}\hat{z} \tag{4.2}$$

where m_u is the magnetic moment of uniform component parallel to B_{ext} and m_h the magnetic moment of helix, both dependent of the intensity of the applied field and temperature, expressed in units of the bohr magneton. In our particular case, the phase ϕ_γ equals -2º if $\gamma = 1$ and 0º otherwise, representing the de-phasing of one helix versus the other three. The $\pm$ stands for the left-handed helicity $(-)$ or right handed helicity $(+)$. Notice the coordinate system used

in this equation corresponds to the one we used in Figure 3.2. The values used for the magnetic moment m , from which m_u and m_h are calculated are $m(T = 2K) = 0.4$, $m(T = 10K) = 0.393$ and $m(T = 28K) = 0.283$ in Bohr magneton units. In order to facilitate equations in the future we are going to define $\vec{m}_c = m_h\hat{x}$ and $\vec{m}_s = m_h\hat{y}$ to re-write:

$$\vec{m}_{dm} = \{\vec{m}_c \vec{S}^{Real}_{\vec{k},d_m} \cos(K_{d,d_m} + \phi_\gamma) \pm \vec{m}_s \vec{S}^{Imag}_{\vec{k},d_m} \sin(K_{d,d_m} + \phi_\gamma)\} + m_u \vec{B_{ext}}, z \tag{4.3}$$

The position of every manganese dm along with their magnetic moment $\vec{m}_{dm}$ is kept on a matrix. The graphic representation of the magnetic moment of the "Mn 1" along the [111] direction of the sample, simulated by the program, is shown in Figure 4.5.

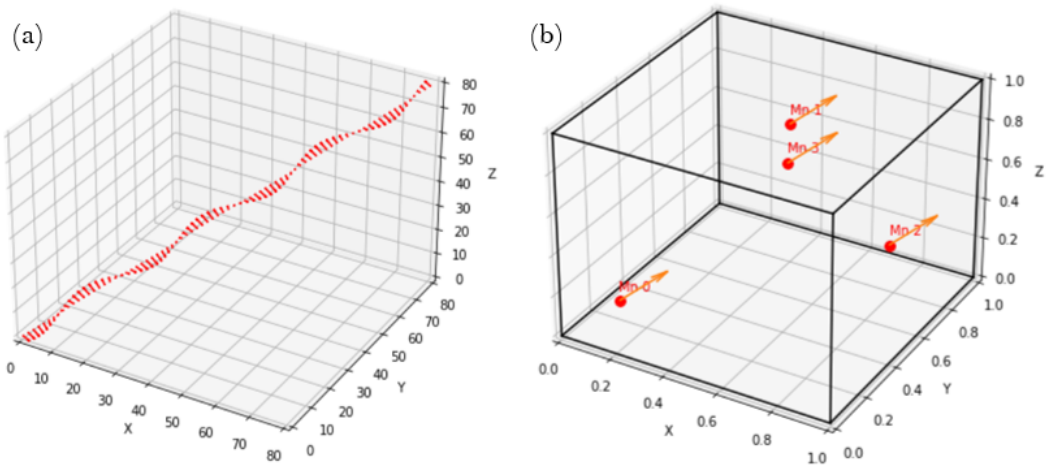

Figure 4.5: (a) Representation of the $\vec{m}_h$ of Mn with Wycoff position $(0.138, 0.138, 0.138)$ along the [111] direction. (b) Representation of the four Mn atoms in the unit cell (labeled in red) and their respective $\vec{m}_u$ (orange).

4.3 Muon implantation site

Just like the position on which Mn atoms locate inside the unit cell, we can define the position d_μ on which the muons implant inside the crystal. Because of its positive electric charge, the muon is implanted in an interstitial site that can be calculated ???. In our case, the muon is located at the Wyckoff position 4a with $x_\mu = 0.532$. This positions are labeled as η.

$$\begin{gathered}
\vec{d_\mu}(\eta = 1) \Longrightarrow (x_\mu, x_\mu, x_\mu) \\
\vec{d_\mu}(\eta = 2) \Longrightarrow (\tfrac{3}{2} - x_\mu, 1 - x_\mu, \tfrac{1}{2} + x_\mu - 1) \\
\vec{d_\mu}(\eta = 3) \Longrightarrow (1 - x_\mu, \tfrac{1}{2} + x_\mu - 1, \tfrac{3}{2} - x_\mu) \\
\vec{d_\mu}(\eta = 4) \Longrightarrow (\tfrac{1}{2} + x_\mu - 1, \tfrac{1}{2} - x_\mu, 1 - x_\mu)
\end{gathered}$$

Besides the position, it is important to know the initial spin polarization of the muon. Muons are spin polarized opposite to their momentum, so when a muon is transported down the beam line, it arrives nearly perfectly spin polarized. We fix the initial polarization of S_μ to the direction defined by $\theta_\mu = \frac{1}{2}\pi$ and ϕ_μ, where θ_μ is the polar angle of the muon spin at the moment of implantation and ϕ_μ the azimutal angle, dependant on the applied magnetic field $\vec{B}_{ext}$.

4.4 Local field at muon's site

The calculation of the intensity and direction of the magnetic field at the muon's site $\vec{B}_{loc}$ is the rough part of building this simulation. In order to imagine what the muon perceives before

decaying we have to take into account several interactions between muon and sample, direct and indirect, that we have reduced to:

$$\vec{B}_{loc} = \vec{B}_{ext} + \vec{B}_{dem} + \vec{B}_{RKKY} + \vec{B}_{dip} + \vec{B}_{Lor} \tag{4.4}$$

It is worth mentioning that Fermi's magnetic field $\vec{B}_{Fermi}$ that represents the muon's interaction with the electronic density at its site (conduction electrons) has been left out, following the thoughts of several studies regarding MnSi samples[7][8].

During the following subsections, every magnetic field taken into account, except for the externally applied one $\vec{B}_{ext}$, is going to be calculated for a muon η located on a unit cell in the center of the sample. One extra section will develop the transformation of this result to every muon's site on the sample, in a way that avoids an endless loop through all of them re-calculating each field.

4.4.1 Demagnetisation Field. $\vec{B}_{dem}$

Every magnetic material has a demagnetisation field. The form anisotropy of a magnetic sample has its origin on the sample's geometry and is defined by the demagnetisation factor tensor $\tilde{\mathbf{N}}$. This effect consists on the creation of a magnetic field $\vec{B}_dem$ opposed to the total magnetization $\vec{M}$ of the sample, following equation 4.5. This means that the muon does not perceive the whole applied field, but a smaller effective field dependant on the sample's geometry.

$$\vec{B}_{dem} = -\tilde{\mathbf{N}}\mu_0\mu_B\frac{4\vec{M}}{a^3} \tag{4.5}$$

where a is the lattice constant and μ_B is Bohr's magneton. Depending on the direction on which we apply the external field, the tensor $\tilde{\mathbf{N}}$ will take a different value. In this simulation we have used the experimental value $N_a = N_b = N_c = 0.55$ [9] where N_a, N_b, N_c are the diagonal values of the tensor.

4.4.2 Hyperfine Field. $\vec{B}_{RKKY}$

Compounds with unpaired "d" electrons have a higher electronic density at the ion's site than between sites, which can be translated into localized magnetic density at crystal sites. This localized electrons' magnetic moments are going to interact with that of the muon in two different ways: the classical dipole interaction and, in metals, through the Ruderman–Kittel–Kasuya–Yosida (RKKY) interaction.

The RKKY is a indirect exchange that describes the interaction between the muon magnetic moment and the magnetic moments of close unpaired electrons through conduction electrons. Since the interaction is at a local level, we limit the calculus to a sphere of radius equal to the lattice constant.

Following equation 4.6, for each muon η of a given unit cell located at the center of the sample, defined by the position $\vec{r}_\eta$, the simulation runs through every manganese atom γ defined by $\vec{r}_\gamma$ that fulfils the condition $|\vec{r}_\eta - \vec{r}_\gamma| \leq a$ and adds up their magnetization $\vec{m}_{dm}$ obtaining $\vec{M}_{average} = \frac{\sum \vec{m}_{dm}}{N'}$.

$$\vec{B}_{RKKY}(\eta) = \frac{\mu_0}{4\pi}\sum_{dm=1}^{N'}\frac{\vec{m}_{dm}}{V_c}\frac{V_{mol}H_{RKKY}}{N'} \tag{4.6}$$

The volume of the unit cell V_c and the volume of a mol of MnSi V_{mol} are known experimental parameters, as well as the RKKY constant $H_{RKKY} = -0.9276\frac{mol}{emu}$. N' stands for the number of manganese atoms that fulfil $|\vec{r}_\eta - \vec{r}_\gamma| \leq a$.

4.4.3 Dipolar Field. $\vec{B}_{dip}$

Another interaction between the magnetic moment of localized "d" unpaired electrons and the magnetic moment of the muon is the long range classic dipole interaction. The dipolar field calculated at the site of a given muon η, $\vec{B}_{dip}(\eta)$, is expressed as a sum of contributions from magnetic moments $\vec{m}_{dm}$ over the whole crystal, as shown in equation 4.7. The distance between the η muon and the γ manganese atom is defined as $\vec{r}_{dm} = \vec{r}_\eta - \vec{r}_\gamma$. The field created by a moment at distance r_{dm} decreases with r_{dm}^{-3}, while the number of moments at that distance increases with r_{dm}^2, which means that the sum does not converge.

$$\vec{B}_{dip}(\eta) = \frac{\mu_0}{4\pi} \sum_{dm=1}^{N} \left[-\frac{\vec{m}_{dm}}{r_{dm}^3} + \frac{3(\vec{m}_{dm}\vec{r}_{dm})\vec{r}_{dm}}{r_{dm}^5} \right] \tag{4.7}$$

This can be solved restricting the sum inside a sphere centered in r_η with a radius big enough so that the lattice sum convergence is reached. This sphere is called the Lorentz sphere with radius $R_{Lorentz} = 90\mathring{A}$ in our simulation.

The same procedure used to calculate the hyperfine field is followed here. For a given muon η located at the center of the sample, defined by $\vec{r}_\eta$, the program runs through every magnetic moment $\vec{m}_{dm}$ at $\vec{r}_{dm}$ that respects the condition $|\vec{r}_\eta - \vec{r}_i| \leq R_{Lorentz}$ while applying equation 4.7.

4.4.4 Lorentz Field. $\vec{B}_{Lor}$

Another part of the dipole interaction is the contribution of the "surface" of the Lorentz sphere, or more precisely, the vector sum of dipoles located inside the Lorentz sphere. For this we need to add all the magnetic moments inside the sphere and then divide them by the volume of the sphere, as expressed in the following equation:

$$\vec{B}_{Lor}(\eta) = \frac{\mu_0}{3} \sum_{V_{Lor}} \frac{\vec{m}_{dm}}{V_{Lor}} \tag{4.8}$$

With this contributions, we can imagine the local field at the center of the sample for a muon η as depicted in Figure 4.6.

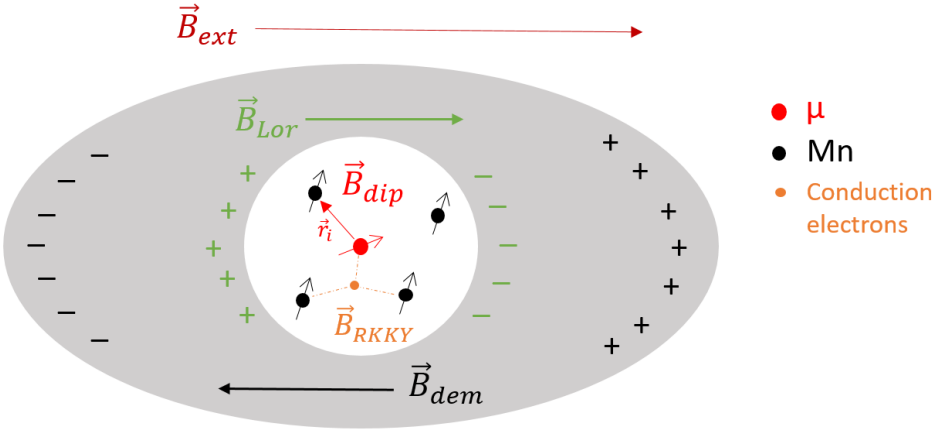

Figure 4.6: Representation of sample (grey) with the Lorentz sphere (white) centered on a muon, with every field that contributes to $\vec{B}_{loc}$ skecthed.

4.4.5 Total Field. $\vec{B}_{loc}$

The previous formulas were written for a specific muon site $\vec{r}_\eta$ at some point along the $\langle 111\rangle$ direction. If we need to obtain the value of each field, for every muon site in every unit cell of the sample, the length of those calculations would consume enormous amounts of time. The path we are going to follow instead tries to minimize the number of re-calculations we need, taking advantage of the periodicity of the helical structure. Suppose we have already calculated the $\vec{B}_{loc}$ at $\vec{r}_\mu$, using the formulas from sections 4.4.1 4.4.3 4.4.4 and 4.4.2 where $\vec{m}_{dm}$ had previously been calculated in equation 4.3.

If we restrict to the plane perpendicular to the propagation direction, the movement would be defined by $(a\langle\bar{1}10\rangle + b\langle\bar{1}\bar{1}2\rangle)$ being "a" and "b" integer numbers. If we take the position of the d_m manganese atom at the d unit cell $\vec{R}_{d,d_m}$ and the implantation position of the muon $\vec{r}_\eta$, the distance between them $r = |\vec{r}_\eta - \vec{R}_{d,d_m}|$ and move both of them along the $a\langle\bar{1}10\rangle + b\langle\bar{1}\bar{1}2\rangle$ plane to a new position $\vec{R}_{d',d_m}$ and $\vec{r'}_\eta$ so that the distance r stays the same, neither the propagation vector, nor the magnetization at muon's site (see 4.2), change.

$$K_{d',d_m} = \vec{K}\vec{R}_{d',d_m} = \vec{K}\vec{R}_{d,d_m} + K(1,1,1)(-a-b, a-b, 2b) = \vec{K}\vec{R}_{d,d_m} \tag{4.9}$$

This means that we only need to evaluate the muon implanted along the $\langle 111\rangle$ direction, since moving along the perpendicular plane does not affect the result. Next, for evaluating the magnetization on a cell $d+h$ along the $\langle 111\rangle$ direction, we can do so by applying the following equation:

$$\begin{aligned}\vec{M}_{d+h,dm} = &[\vec{m}_c\cos(K_{d,d_m}) - \vec{m}_s\sin(K_{d,d_m})]\cos(\vec{K}\vec{x}_h + \phi_{dm})\\ &- [\vec{m}_c\sin(K_{d,d_m}) + \vec{m}_s\cos(K_{d,d_m})]\sin(\vec{K}\vec{x}_h + \phi_{dm})\\ &+ m_u\vec{B}_{ext}\end{aligned}$$

where $\vec{x}_h = (h,h,h)$ would move forward in the propagation direction $\langle 111\rangle$ from the d unit cell to the $d+h$ unit cell. If we name this movement forward as $\beta = \vec{K}\vec{x}_h$ and define $\vec{M}_{B_c}$, $\vec{M}_{B_s}$ and $\vec{M}_{B_u}$ as:

$$\begin{aligned}\vec{M}_{Bc} &= [\vec{m}_c\cos(K_{d,d_m}) - \vec{m}_s\sin(K_{d,d_m})]\\ \vec{M}_{Bs} &= -[\vec{m}_c\sin(K_{d,d_m}) + \vec{m}_s\cos(K_{d,d_m})]\\ \vec{M}_{Bu} &= m_u\vec{B}_{ext}\end{aligned}$$

we get the final equation describing $\vec{B}_{loc}(\gamma)$ for a muon η produced by the γ-type magnanese atoms around it as:

$$\vec{B}_{loc}(\gamma) = \vec{B}_{ext} + \vec{B}_{dem} + \vec{B}_c(\gamma)\cos(\beta+\phi_{dm}) + \vec{B}_s(\gamma)\sin(\beta+\phi_{dm}) + \vec{B}_u(\gamma) \tag{4.10}$$

This way, as an example, the $\vec{B}_{Lor,c}(\eta)$ would be obtained by substituting $\vec{M}_{B_c}$ in the Lorentz equation 4.8. This way, repeating the process with the other fields:

$$\vec{B}_c(\gamma) = \vec{B}_{Lor,c}(\gamma) + \vec{B}_{RKKY,c}(\gamma) + \vec{B}_{Dip,c}(\gamma) \tag{4.11}$$

The sum to all four γ manganese, with $\phi(\gamma=1)$ = -2º and $\phi(\gamma=2,3,4)$ =0º provides the final local field at the muon site, $\vec{B}_{loc}$.

In summary, we have achieved a way of calculating the different fields at each muon site for a cell located in the middle of the sample, while being able to obtain the $\vec{B}_{loc}$ at any point in the propagation direction and any point on its perpendicular planes.

4.5 Larmor equation

Once the field at the muon's site $\vec{B}_{loc}$ is calculated, we use it to simulate the change of the muon's spin polarization $\vec{S}_\mu$. This is achieved by applying the Larmor equation, as explained in Chapter 2. The expression for the final polarization used the Cartesian components of the $\mathbf{M}(t)$ tensor (equation 3.9). If we substitute the longitudinal and transverse operators $\mathbf{P}_L$, $\mathbf{P}_{T1}$ and $\mathbf{P}_{T2}$ (defined on [7] Section C.1) and, in order to simplify the notation, we label the module of $\vec{B}_{loc}$ as B and its Cartesian components as $\vec{B}_\alpha, \vec{B}_\beta, \vec{B}_\gamma$, we arrive to:

$$M^{\alpha\alpha}(t) = \frac{\vec{B}_\alpha^2}{B^2} e^{-\lambda_z t} + \left[1 - \frac{\vec{B}_\alpha^2}{B^2}\right] \cos(\omega t) e^{-Gt^2 - \lambda_x t} \tag{4.12}$$

$$M^{\alpha\beta}(t) = \frac{\vec{B}_\alpha \times \vec{B}_\beta}{B^2} \left[1 - \cos(\omega t)\right] e^{-Gt^2 - \lambda_x t} + \frac{\vec{B}_\gamma}{B} \sin(\omega t) e^{-Gt^2 - \lambda_x t} \tag{4.13}$$

$$M^{\alpha\gamma}(t) = \frac{\vec{B}_\alpha \times \vec{B}_\gamma}{B^2} \left[1 - \cos(\omega t)\right] e^{-Gt^2 - \lambda_x t} + \frac{\vec{B}_\beta}{B} \sin(\omega t) e^{-Gt^2 - \lambda_x t} \tag{4.14}$$

In expressions 4.124.134.15 spin relaxation has been taken into account. This physical phenomena describes the gradual loss of the spin orientation in the static field $\vec{B}_{loc}$ [10]. We can distinguish spin–lattice relaxation, expressed through $\lambda_z = 0.03 \mu s^{-1}$ and related to the lattice vibrations of surrounding atoms and spin–spin relaxation, expressed through $\lambda_x = 2 \mu s^{-1}$ and related to the fact that interactions between nearby spins tend to destroy the phase coherence in the Larmor precession. We also consider other effects like the muon being mobile (not perfectly fixed) or the effect of the neighboring spins fluctuating strongly and averaging out the local fields. This leads a damping of the external field precession described by a Gaussian-type factor "Gauss factor" G:

$$G = \frac{1}{2} \gamma_\mu^2 \delta^2 \tag{4.15}$$

where γ_μ is the muon gyromagnetic ratio, $\gamma_\mu = 851.616 \times 10^6 \frac{rad}{sT}$ and $\delta = 0.0008T$ stands for the root-mean-square of a Gaussian field distribution.

After the components of the $\mathbf{M}(t)$ tensor are known, the change in polarization can be expressed as follows:

$$\vec{S}^\alpha(t) = M^{\alpha\alpha}(t) \cos(\phi_\mu) \sin(\theta_\mu) + M^{\alpha\beta}(t) \sin(\phi_\mu) \sin(\theta_\mu) + M^{\alpha\gamma}(t) \cos(\theta_\mu) \tag{4.16}$$

Chapter 5

First results and future work

The raw result of a $TF - \mu SR$ experiment looks like the left graph on Figure 5.1 by building a histogram of the detected positron as a function of time. Then the background signal (time-independent and beam-dependent) is removed and the radioactive exponential decay component is corrected and the polarization normalized, in order to obtain the graph on the right.

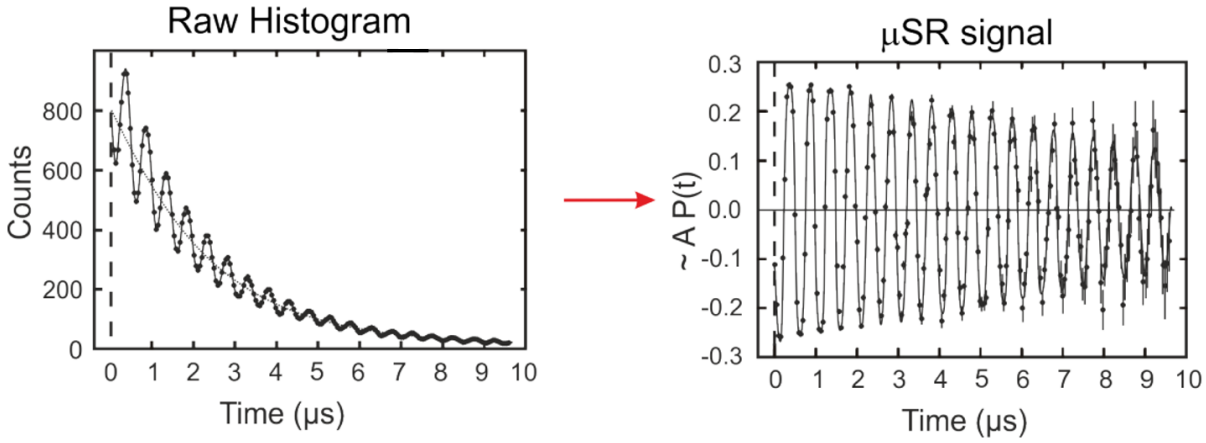

Figure 5.1: Direct result of $TF - \mu SR$ experiment and treated polarization signal

The spectre we are left with presents oscillations originated due to the Larmor precession of the muon spin around the local field. The frequency of the oscillation depends on the local field at the muon site, so that a change from time to frequency facilitates reading the physical information attained by this measurements. The transformation from time to frequency (related to magnetic local field) is done via the Fourier Fast Transformation (FFT). Plotting the FFT against frequency $\sim B_{loc}$ peaks will signal the values of the magnetic field (or fields) the muon senses before decaying. In order to understand this better, let us imagine a simple example: if we considered a magnetically homogeneous sample, there would only be one magnetic field, so that the muons stopping at any site of the sample would sense the same B_{loc} and precess that field with the same Larmor frequency, creating only one FFT peak. If the sample were to be inhomogeneous, depending on factors like the implantation site the modeule of the local field would change, resulting in muon spins precessing at different frequencies, creating several peaks with different amplitudes.

The respective amplitudes of different peaks account for the proportion of muons that sense one value or another. The amplitude of the FFT not only gives us the module of the local magnetic field, but will also allow us to compare it to other experimental settup geometries and obtain the direction of said field. Applied external field or temperature also modify the position and number of peaks, since B_{loc} is strongly affected by B_{ext}

So far we have discussed "peaks" as if they were ideal, but their width also holds important information. Parameters introduced in the previous section like relaxation factors. Real samples also carry some instrinsic disorder in comparison with theoretical ideal ones, so that a distribution (Figure 5.2) of the fields around a mean value $\langle B_\mu \rangle$ is produced (Gaussian distribution, for further explanation see [11]).

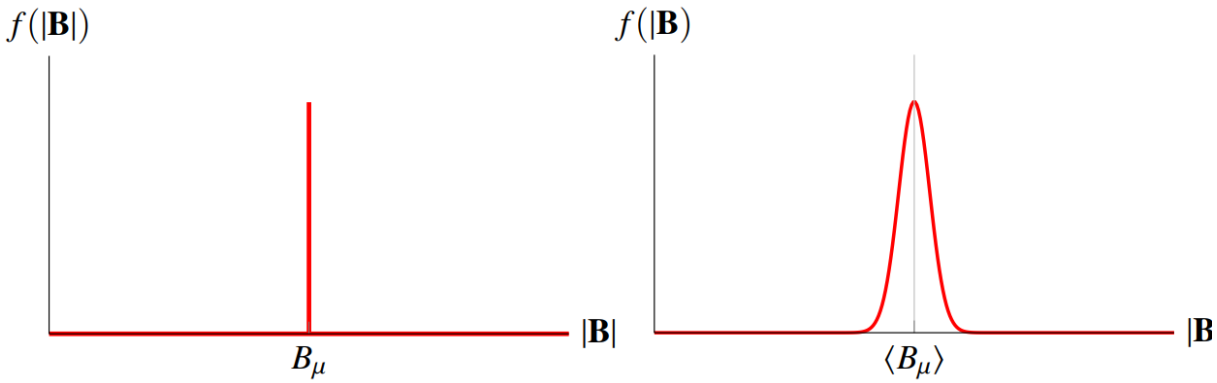

Figure 5.2: Left: ideal field distribution for the field value. Right: more real distribution with a width determined by the Gaussian distribution

While working with "simpler" samples the analysis of the results can be achieved, in samples with a certain level of complexity it is advantageous, if not necessary, to design a simulation of the experiment. This way simulated and real results can be compared and, by varying our model, we can discover the contribution each of our parameters has on the final outcome, a connection incredibly hard to draw by just analyzing the experimental results.

The simulation software described on the previous chapter has been used for modelling a μSR experiment at a temperature of 2K and different values of applied external magnetic field. The simulated final averaged polarisation has been plotted against time and compared to the experimental final polarisation (left column of Figure 5.3).

Both the simulation and experimental data have been equally treated and the Fourier Fast Transform has been obtained (right column of Figure 5.3).

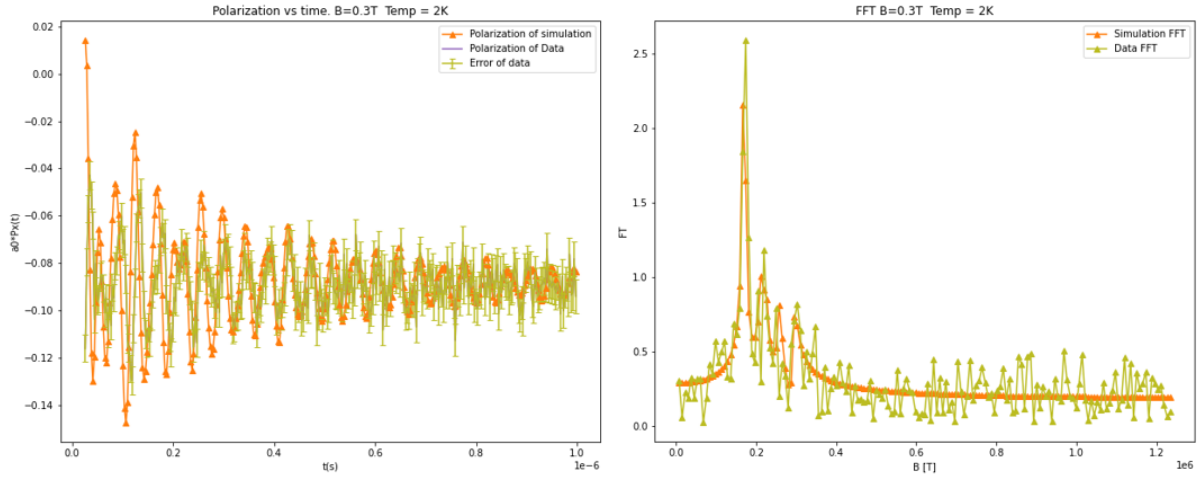

Figure 5.3: Simulation vs experimental results comparison- 2K and B = 0.03T

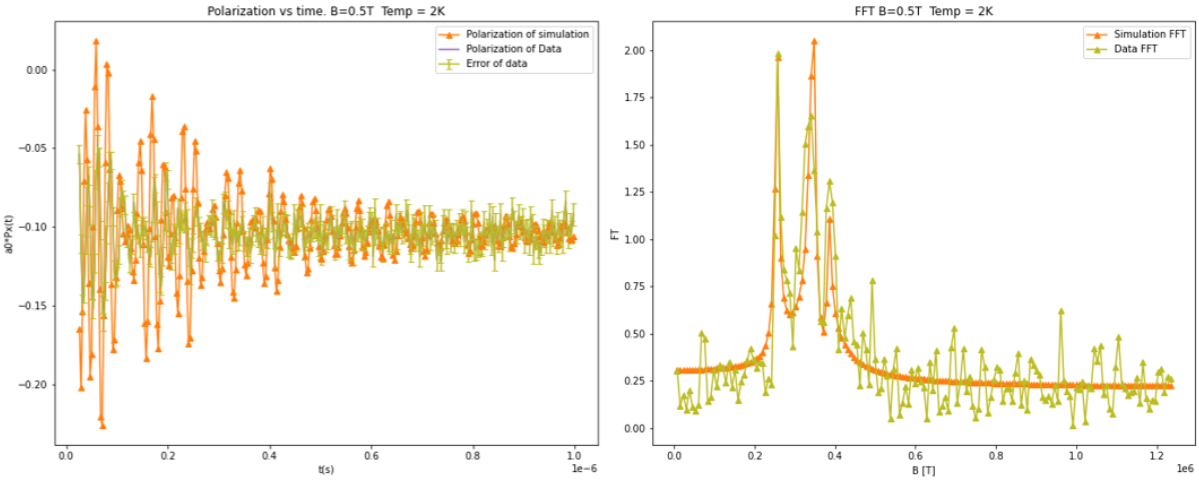

Figure 5.4: Simulation vs experimental results comparison. 2K and B = 0.05T

The intensity of the FFT peaks of the simulation results has been multiplied by a 0.15 factor with the objective of facilitating the comparison between peaks positions. The FFT has been represented against the magnetic field. We can clearly appreciate how close both results are, implying the design of the simulation can be considered trustworthy.

Now that the simulation is finished, several steps can be taken. On one hand, the simulation could always be improved. The simulated results are close enough to the experimental ones but a better depolarization effect should be achieved by the model. On the other hand, this simulation, although already shapable in terms of muon implantation sites and nuclear struture, only has two magnetic models programmed (simple ferromagnetic and helicoid ferromagnetic). The final goal is to simulate the muon signal for any magnetic structure, for that it is foreseen to use the general magnetic crystallographic file (mCIF) as an entry to our code. In the same line, other experimental geometries besides TF should also be considered. While many other experimental techniques have a wide range of data simulation and data treatment programs, very few (if any at all) exist nowadays as a universal μSR simulating software. Moreover, we intend to use our simulation module as a function to be employed in a least square minimization routine to be able to fit the parameters of the model.

The fitting process will detail the theorised model and give insight on its level of goodness, besides refining the theorised value of the parameters used. Then, once the treatment of the data is finished, the actual analysis can begin

Over all, this work provides a strong tool for future magnetic research, since other magnetic models could be added to it and many "customizable" options are already incorporated to it. On the learning part, not only has it required achieving a deep understanding of a completely new experimental technique for me, an understanding that I dare say has gone deeper than the one needed for solely applying the technique, but it has also made me see the importance of using complementary techniques in experimental science. It has given me the great experience of following over several years the work of the M4 research group working on the same set of samples from different perspectives, from the first magnetometry characterizations, to the SANS data treatment and now μSR experiments and simulations, I have seen them combining experimental techniques, programming resources and, after every step, re-thinking what the following course of action will be. I have enjoyed being able to contribute with this code and definitely look forward to seeing it evolve as new contributions are added.

Appendix A

Pyhton Code

Definition of Manganese nuclear structure parameters:

```
R = ([[1,0,0],[0,1,0],[0,0,1]]) # Vector of cubic unit cell
x_Mn = float(Var['x_Mn'])       # Possition of Mn in unit cell
a_1 = float(Var['a_1'])         # Lattice constant
Cellm = float(Var['Cellm'])     # Number of unit cells for muons

# 4Mn sublattices in unit cell
v1 = ([[x_Mn, x_Mn, x_Mn], [0.5-x_Mn, 1-x_Mn, 0.5+x_Mn],
    [1-x_Mn, 0.5+x_Mn, 0.5-x_Mn], [0.5+x_Mn, 0.5-x_Mn, 1-x_Mn]])
d_Mn = a_1* v1
```

Definition of Manganese magnetic structure:

```
kmod = float(Var['kmod'])/(2*pi)   # Modulus of propagation vector
phid = np.array(Var['phid'])       # phase on the 4 Mn

if (Var['MagPh']==1):

    #Defines FouReal on X-axis, Fou imag on Y-axis and kdir on Z-Axis
    # kdir = direction of propagation vector
    kdir = (Var['FouReal'])* sin(Rotang) + (Var['kdir'])*cos(Rotang)
    n = kdir/np.linalg.norm(kdir)  # unitary
    k = kmod*n  # Propagation vector
    FouReal = (Var['FouReal'])* cos(Rotang) - Var['kdir'])*sin(Rotang)
    FouImag = (Var['FouImag'])
    #Fourier coeff
    S1 = FouReal/norm(FouReal) + 1j *FouImag/norm(FouImag)
    m_h, m_u = M_Moment_u(Var['Temp']),(Var['Bext']),(Var['m']))
```

Calculation of Manganese magnetic moments following the 4 helix model:

```
Cell = int(Var['Cellm'])
Mdem = 0
Lima = round(Var['Lor_rad']/Var['a_1'])
                        # The K1Ri will point to a specific cell
k1R1 = 2*pi*Var['a_1']*k@R[0].reshape(-1,1)   # R[0] = (000)
k1R2 = 2*pi*Var['a_1']*k@R[1].reshape(-1,1)   # R[1] = (010)
k1R3 = 2*pi*Var['a_1']*k@R[2].reshape(-1,1)   # R[2] = (001)

for dm in range(4):       # We go through all of the four Mn
```

```
    kr =  np.transpose(2*pi*k@(d_Mn[dm]))
    d=0
    Limbcd = 0
    Limbcup = 4*Lima
    for ai in range(Cell):
    # ai goes throught the 80 cells
        if (ai > 2*Lima and ai < Cell - 2*Lima):
            Limbcd = ai - 2*Lima
            Limbcup = ai + 2*Lima
        for bi in range(Limbcd, Limbcup):
            for ci in range(Limbcd, Limbcup):
            # Sum to every cell
                # K1Ri gives the cell, kr the Mn
                k1x = k1R1*ai + k1R2*bi + k1R3*ci + kr

                Mnorm[0] = m_h*(real(S1)*cos(k1x) - imag(S1)*sin(k1x))
                # - for left-handed helicity, + for right
                Mc[dm][ai][bi][ci] = Mnorm[0]
                Ms[dm][ai][bi][ci] = -m_h*(real(S1)*sin(k1x)
                        + imag(S1)*cos(k1x))
                #+ for left-handed helicity, - for right
                Mu[dm][ai][bi][ci] = m_u * Bdir
                Mdem = Mnorm[0] + m_u * Bdir + Mdem
                Pos[0]= Var['a_1']*(R[0]*ai + R[1]*bi
                        + R[2]*ci) + d_Mn[dm]
                P[dm][ai][bi][ci] = Pos[0] #Mn in cell(ai,bi,ci)
                CellVis[dm][d]= U@Pos[0]
                MVis[dm][d] = U@(Mnorm[0] + m_u*Bdir)
                d = d+1

Mdem = Mdem /(4*d)
```

Definition of muon implantation parameters:

```
x_mu = float(Var['x_mu'])
v3 = ([[x_mu, x_mu, x_mu], [1.5-x_mu, 1-x_mu, 0.5+x_mu-1],
[1-x_mu, 0.5+x_mu-1, 1.5-x_mu], [0.5+x_mu-1, 1.5-x_mu, 1-x_mu]])
d_mu = a_1*v3
L = Var['L']
v4 = [[-1,-1,-1], [-1,-1,-1], [-1,-1,-1], [-1,-1,-1]]

delta_t = 10**(-9)
gamma_L = 851.616*(10**6)  # Muon gyromagnetic ratio [rad/(s*T)]
theta_mu = Var['theta_mu']*pi  # polar angle of the muon spin
                                 at the moment of implantation
phi_mu = Var['phi_mu']*pi      # azimuthal angle of the muon spin
                                 at the moment of implantation.
                                 Depends on B_ext
Lambda_z = Var['Lambda_z']*(10**6) #long. dynamical relaxation [1/s]
Lambda_x = Var['Lambda_x']*(10**6) #Damping induced by magnetic
                                     fluctuations [1/s]
Delta_N = (Var['Delta_N'])     # Root-mean-square of a Gaussian field
```

```
                                    distribution [T]
Gaus = (gamma_L**2)*(Delta_N**2)/2
Lambda_bg = Var['Lambda_bg']*(10**6) #Background relaxation rate [1/s]
a_0 = Var['a_0']                     # Initial asymmetry factor
B_ext = Var['Bext']*Bdir             # Magnetic field applied [T]
```

Definition of variables for the calculation of the magnetic field at the muon site:

```
# Definition of variables

mu_B = 9.27401*(10**(-24))       # Bohr magneton [J/T]
mu_0 = 4*pi*(10**(-7))
Acont = Var['Acont']       # [mol/emu], related to hyperfine constant H
Vmol = (Var['a_1']**3)*6.022*0.1/4  # volume of one mol of
                                      Mn-ions [cm^3/mol]
Cnt = Vmol*Var['Acont']*4/(Var['a_1']**3)  # [1/A^3]

Lor = (mu_0*mu_B*(10**30)/(3*Lor_vol))
Dip = (mu_0*mu_B*(10**30)/(4*pi))
```

Demagnetization field:

```
N = Var['N']
B_dem = -N*mu_0*((4*Mdem*mu_B)/((Var['a_1']**(3)*(10**(-30)))))
```

Hyperfine field:

```
Lim = 1
a = b = c = (Cellm/2)-1

for eta in range(4):
    Ri = d_mu[eta] + Var['a_1']*(R[0]*a + R[1]*b + R[2]*c)
    # Where d_mu is the position of the muon eta
    for gamma in range(4):    # We calculate for every Mn gamma
        C = 0
        Msumc = 0
        Msums = 0
        Msumu = 0
        for ai in range (-Lim,Lim+1):
            for bi in range (-Lim,Lim+1):    # Sum to each l-th cell
                for ci in range (-Lim,Lim+1):
                    Ps[0] = P[gamma][int(a+ai)][int(b+bi)][int(c+ci)]
                    # Distance from muon eta to Mn gamma
                    Dif[0] = Ri - Ps
                    if np.linalg.norm(Dif) < Var['a_1']:
                    #If closer than the cell parameter they add to M
                        C = C + 1
                        MDc[0] =
                          Mc[gamma][int(a+ai)][int(b+bi)][int(c+ci)]
                        Msumc = MDc[0] + Msumc
                        MDs[0] =
                          Ms[gamma][int(a+ai)][int(b+bi)][int(c+ci)]
                        Msums = MDs[0] + Msums
                        MDu[0] =
```

```
                        Mu[gamma][int(a+ai)][int(b+bi)][int(c+ci)]
                    Msumu = MDu[0] + Msumu
        if C == 0:
            Conc[eta][gamma]= Cons[eta][gamma]= Conu[eta][gamma]= 0
        else:
            Conc[eta][gamma] = (1/4)*(float(Cnt)/float(C))*Msumc
            Cons[eta][gamma] = (1/4)*(float(Cnt)/float(C))*Msums
            Conu[eta][gamma] = (1/4)*(float(Cnt)/float(C))*Msumu
    B_cont_cos[eta] = Dip*Conc[eta]
    B_cont_sin[eta] = Dip*Cons[eta]
    B_cont_u[eta] = Dip*Conu[eta]
```

Lorentz and Dipolar fields:

```
Lima = round(Var['Lor_rad']/Var['a_1'])
a = Cell/2 -1

for eta in range(4):
    Ri = d_mu[eta] + Var['a_1']*(R[0]*a + R[1]*a + R[2]*a)
    for gamma in range(4):
        Msum1c =0
        Msum2c =0
        Msum1s =0
        Msum2s =0
        Msum1u =0
        Msum2u =0
        for ai in range (-Lima,Lima+1):
            for bi in range (-Lima,Lima+1): # Sum to each l-th cell
                for ci in range (-Lima,Lima+1):
                    Ps[0] = P[gamma][int(a+ai)][int(a+bi)][int(a+ci)]
                    Dif[0] = Ri - Ps # Distance muon eta - Mn gamma
                    if np.linalg.norm(Dif) < Var['Lor_rad']:
                        MDc[0] =
                          Mc[gamma][int(a+ai)][int(a+bi)][int(a+ci)]
                        Msum1c = MDc[0] + Msum1c
                        MDs[0] =
                          Ms[gamma][int(a+ai)][int(a+bi)][int(a+ci)]
                        Msum1s = MDs[0] + Msum1s
                        MDu[0] =
                          Mu[gamma][int(a+ai)][int(a+bi)][int(a+ci)]
                        Msum1u = MDu[0] + Msum1u

                        Dif3 = np.linalg.norm(Dif)**3
                        Dif5 = np.linalg.norm(Dif)**5

                        Msum2c = -(1/Dif3)*MDc + (3/Dif5)
                          *(MDc@Dif.reshape(-1,1))*Dif + Msum2c
                        Msum2s = -(1/Dif3)*MDs + (3/Dif5)
                          *(MDs@Dif.reshape(-1,1))*Dif + Msum2s
                        Msum2u = -(1/Dif3)*MDu + (3/Dif5)
                          *(MDu@Dif.reshape(-1,1))*Dif + Msum2u
```

```
        H1c[gamma] = Msum1c
        H2c[gamma] = Msum2c
        H1s[gamma] = Msum1s
        H2s[gamma] = Msum2s
        H1u[eta][gamma] = Msum1u
        H2u[eta][gamma] = Msum2u

    B_Lor_cos[eta] = Lor*H1c  # Lorentz field [T]
    B_Lor_sin[eta] = Lor*H1s  # Lorentz field [T]
    B_Lor_u[eta] = Lor*H1u[eta]    # Lorentz field [T]

    B_Dip_cos[eta] = Dip*H2c  # Dipolar field [T]
    B_Dip_sin[eta] = Dip*H2s  # Dipolar field [T]
    B_Dip_u[eta] = Dip*H2u[eta]    # Dipolar field [T]
```

Addition of every field:

```
phi = phid*pi/180
Sxt_d = np.zeros(shape=(4,len(Time)))

for eta in range(4):
    B_cos[eta] = B_Dip_cos[eta] + B_cont_cos[eta] + B_Lor_cos[eta]
    # Addition of dipolar + hyperfine + Lorentz on each muon
    B_sin[eta] = B_Dip_sin[eta] + B_cont_sin[eta] + B_Lor_sin[eta]
    B_u[eta] = B_Dip_u[eta] + B_cont_u[eta] + B_Lor_u[eta]
    B_c = B_cos[eta]
    B_s = B_sin[eta]
    B_u2[eta] = Dip*sum(H2u[eta])
                + Dip*sum(Conu[eta]) + Lor*sum(H1u[eta])
    d = 0
    for alpha in np.arange(0, 2*np.pi + np.pi/180, np.pi/180):
        B = B_ext + B_dem + B_u2[eta] \
            + B_c[0]*cos(alpha+phi[0]) + B_s[0]*sin(alpha+phi[0]) \
            + B_c[1]*cos(alpha+phi[1]) + B_s[1]*sin(alpha+phi[1]) \
            + B_c[2]*cos(alpha+phi[2]) + B_s[2]*sin(alpha+phi[2]) \
            + B_c[3]*cos(alpha+phi[3]) + B_s[3]*sin(alpha+phi[3])
        B = (U@B.reshape(-1,1)).reshape(-1,1)
        B_mod[eta][d] = np.linalg.norm(B)
        omega = gamma_L*B_mod[eta][d]
        d = d + 1;
                                        # model
        for i in range(Var['L']):
            t[i] = i*delta_t
            Sxt_m[eta][i] += \
                  a_0*fun.Larmor(t, i, B, omega,theta_mu, \
                                 phi_mu,Lambda_z,Lambda_x,Gaus)

        B_mod_L = np.linalg.norm(B)
                                        # model in data points
        for i in range(len(Time)):
            t[i] = xdata[i]
```

```
            Sxt_d[eta][i] += a_0*fun.Larmor(St, i, B,\
                    omega,theta_mu,phi_mu,Lambda_z,Lambda_x,Gaus)
            Mxx = ((B[0]**2/B_mod_L**2)*exp(-Lambda_z*t[i])) +\
                        (1-B[0]**2/B_mod_L**2)*cos(omega*t[i])*\
                            exp(-Gaus*t[i]**2-Lambda_x*t[i])
            Mxy = (((B[0]@B[1])/B_mod_L**2)*(1-cos(omega*t[i]))\
                    *exp(-Gaus*t[i]**2-Lambda_x*t[i]) +    \
(B[2]/B_mod_L)*sin(omega*t[i]) \
                                *exp(-Gaus*t[i]**2-Lambda_x*t[i]))
            Mxz = ((B[0]@B[2]/B_mod_L**2)*(1-cos(omega*t[i]))\
                    *exp(-Gaus*t[i]**2-Lambda_x*t[i]) - \
                            (B[1]/B_mod_L)*sin(omega*t[i])\
                                *exp(-Gaus*t[i]**2-Lambda_x*t[i]))
            S = 0.7
            Sxt_d[eta][i] += \
                a_0*float(S*(Mxx*cos(phi_mu)*sin(theta_mu)) +
                    Mxy*sin(phi_mu)*sin(theta_mu) + Mxz*cos(theta_mu))


for i in range(Var['L']):
    S_m[0][i] = (Sxt_m[0][i]+Sxt_m[1][i]+
                 Sxt_m[2][i]+Sxt_m[3][i])/(4*360)
for i in range(len(Time)):  # dim = Time of data
    S_d[0][i] = (Sxt_d[0][i]+Sxt_d[1][i]+
                 Sxt_d[2][i]+Sxt_d[3][i])/(4*360) - 0.11
```

Fast Fourier Transform:

```
Step = xdata[1] - xdata[0]
L2 = len(Time)
Bf_d = np.zeros(L2//2)
Y_d = np.abs(np.fft.fft(S_d[0]))
F_d = 2 * (Y_d[1:L2//2+1])
Ampdata = np.abs(np.fft.fft(ydata))
F_data = 2 * (Ampdata[1:L2//2+1])
for i in range(1, L2//2+1):
    Bf_d[i-1] = i * 2 * np.pi / (851.616 * len(Time) * Step)
```

Bibliography

[1] Victor Laliena and Javier Campo. Stability of skyrmion textures and the role of thermal fluctuations in cubic helimagnets: A new intermediate phase at low temperature. *Physical Review B*, 96(13):134420, 2017.

[2] Sebastian Muhlbauer, Benedikt Binz, F Jonietz, Christian Pfleiderer, Achim Rosch, Anja Neubauer, Robert Georgii, and Peter Boni. Skyrmion lattice in a chiral magnet. *Science*, 323(5916):915–919, 2009.

[3] M Ohkuma, M Mito, M Pardo, Y Kousaka, S Iwasaki, K Ohishi, J Akimitsu, K Inoue, V Laliena, and J Campo. New magnetic intermediate state,"b-phase," in the cubic chiral magnet mnsi. *APL Materials*, 10(4):041104, 2022.

[4] Javier Campo and Víctor Laliena. Neutron scattering in magnetism: Fundamentals and examples. In *Magnetic Measurement Techniques for Materials Characterization*, pages 321–403. Springer, 2021.

[5] Shin-ichi Takata, Jun-ichi Suzuki, Takenao Shinohara, Takayuki Oku, Taiki Tominaga, Kazuki Ohishi, Hiroki Iwase, Takeshi Nakatani, Yasuhiro Inamura, Takayoshi Ito, et al. The design and q resolution of the small and wide angle neutron scattering instrument (taikan) in j-parc. In *Proceedings of the 2nd International Symposium on Science at J-PARC—Unlocking the Mysteries of Life, Matter and the Universe—*, page 036020, 2015.

[6] Kazuki Ohishi, Yusuke Kousaka, Satoshi Iwasaki, Jun Akimitsu, Miguel Pardo-Sainz, Victor Laliena, Javier Campo, Masahiro Ohkuma, and Masaki Mito. *Small Angle Neutron Scattering Study near the Critical Field at Low Temperature in MnSi.*

[7] Alain Yaouanc and Pierre Dalmas De Reotier. *Muon spin rotation, relaxation, and resonance: applications to condensed matter*. Number 147. Oxford University Press, 2011.

[8] Alex Amato, Pierre Dalmas de Réotier, Daniel Andreica, and Alain Yaouanc. Understanding the μsr spectra of mnsi without magnetic polarons. *Phys. Rev. B*, 89:184425, May 2014.

[9] Charles Kittel. Introduction to solid state physics eighth edition. 2021.

[10] Erik B Karlsson. Internal dynamics in condensed matter, as studied by spin relaxation: some examples from 75 years. *The European Physical Journal H*, 47(1):4, 2022.

[11] Alex Amato and Hubertus Luetkens. Physics with muons: From atomic physics to solid state physics, lecture, 2018.